

Multifunctional bandgap-reduced ZnO nanocrystals for photocatalysis, self-cleaning, and antibacterial glass surfaces

Citation

MASAŘ, Milan, Hassan ALI, Ali Can GÜLER, Michal URBÁNEK, Pavel URBÁNEK, Barbora HANULÍKOVÁ, Hana PIŠTĚKOVÁ, Adriana ANNUŠOVÁ, Michal MACHOVSKÝ, and Ivo KUŘITKA. Multifunctional bandgap-reduced ZnO nanocrystals for photocatalysis, self-cleaning, and antibacterial glass surfaces. *Colloids and Surfaces A: Physicochemical and Engineering Aspects* [online]. vol. 656, Elsevier, 2023, [cit. 2024-04-16]. ISSN 0927-7757. Available at <https://www.sciencedirect.com/science/article/pii/S0927775722022026>

DOI

<https://doi.org/10.1016/j.colsurfa.2022.130447>

Permanent link

<https://publikace.k.utb.cz/handle/10563/1011260>

This document is the Accepted Manuscript version of the article that can be shared via institutional repository.



TBU Publications

Repository of TBU Publications

publikace.k.utb.cz

Multifunctional bandgap-reduced ZnO nanocrystals for photocatalysis, self-cleaning, and antibacterial glass surfaces

Milan Masar^a, Hassan Ali^a, Ali Can Guler^a, Michal Urbanek^a, Pavel Urbanek^a, Barbora Hanulikova^a, Hana Pistekova^a, Adriana Annusova^{b,c}, Michal Machovsky^{a,*}, Ivo Kuritka^a

^aCentre of Polymer Systems, Tomas Bata University in Zlin, Tr. Tomase Bati 5678, 760 01 Zlin, Czech Republic

^bDepartment of Multilayers and Nanostructures, Institute of Physics, Slovak Academy of Sciences, Dúbravská cesta 9, 845 11 Bratislava, Slovakia

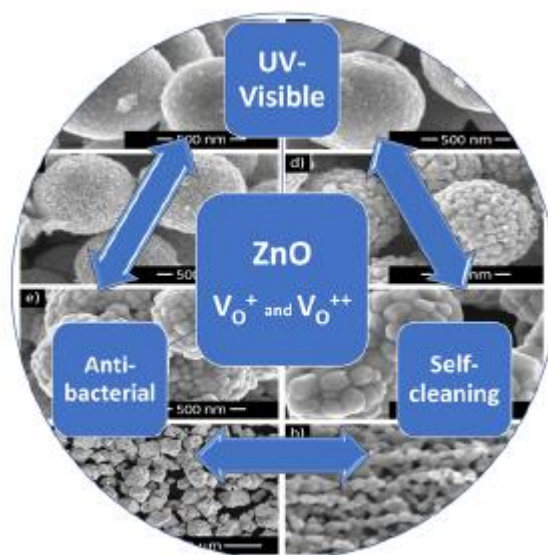
^cCentre for Advanced Materials Application, Slovak Academy of Sciences, Dúbravska cesta 9, 845 11 Bratislava, Slovakia

*Corresponding author: E-mail address: machovsky@utb.cz (M. Machovsky).

HIGHLIGHTS

- Method for preparation of ZnO nanocrystals assembly with tunable bandgap proposed.
- Oxygen vacancies introduced uniquely during phase transformation from ZnO₂ to ZnO.
- Bandgap narrowing due to oxygen vacancies elucidated by EPR and Raman.
- Photocatalytic, self-cleaning, antibacterial property glass-coating demonstrated.

GRAPHICAL ABSTRACT



ABSTRACT

A set of ZnO nanocrystals assembly with tuneable reduced bandgaps was prepared via thermal decomposition of ZnO₂ precursor. A detailed Raman and EPR analysis revealed ZnO rich in oxygen vacancies with concentration varying upon annealing temperature. The structural defect features

corroborated with the bandgap variations indicate photocatalytic response in the visible-light, which was evaluated by using monochromatic LEDs (377, 401, and 429 nm wavelengths) for a correct assessment of the photocatalytic activities of samples in the close vicinities of their bandgaps. It was revealed, that bandgap reduced ZnO exhibits only little yet negligible photocatalytic activity towards Methylene Blue discoloration under 429 nm diode. The Photocatalytic experiments using scavengers support the model that oxygen vacancies easily trap photo-excited electrons (whether V_0^+ and V_0^{++} state) and, if the energy level of this donor state is close enough, the trapped electron could easily thermalize to the conduction band as well as recombine with photo-excited holes. Furthermore, oxygen vacancies rich ZnO nanocrystals treated glasses were prepared and their photocatalytic-induced self-cleaning property, wettability, and antibacterial activities were evaluated under both UV and visible-light. Besides excellent antibacterial

Keywords: ZnO, oxygen vacancy, photocatalysis, antibacterial, self-cleaning, glass

1. Introduction

Semiconductor-based photocatalysis has generated much scientific interest due to its potential application in renewable energy and environmental remediation [1]. Although water splitting has been the main focus of photocatalysis, many applications have appeared recently. The design of multifunctional semiconducting self-cleaning, superhydrophilic, antifogging, and antimicrobial surfaces is based on the reaction pathway, which is activated by the absorption of photons with energy equal to or higher than the energy bandgap of the semiconductor [2,3]. Titanium dioxide and zinc oxide are historically by far the most explored photocatalysts possessing wide bandgaps and thus implying the necessity of UV light irradiation ($\lambda < 400$ nm) for activation. UV light accounts for only 5% of the solar spectrum, whereas visible light contributes approximately 40%, making the visible-light responsive photocatalysts highly desirable [4]. Extensive efforts have been made to develop visible light-activated photocatalysts and are documented in comprehensive reviews[5,6]. Besides dye anchoring [7], coupling with narrow bandgap semiconductor or carbonaceous materials [8,9], metal nanoparticle decoration can be used for extending the light absorption range [10]. Unlike previous methods, bandgap engineering is the most common method of narrowing the bandgap of semiconductors either by non-metal or metal doping [11,12], including co-doping [13]. However, a suitably controlled doping of nanomaterials is difficult as it is influenced not only by the method employed, but is also very sensitive to many parameters within a specific method and the temperature profile of the subsequent post-thermal treatment [14]. Moreover, the optimum doping ratio for a given element varies from photocatalyst to photocatalyst, although a general predictive model for optimum doping ratio was proposed [15].

Manipulation of native point defects in the crystal lattice, so-called defect engineering, has been reported as an effective strategy for enhancing photocatalytic activities of TiO_2 and ZnO by extending the light absorption to the visible light spectrum [16,17]. Specifically, in ZnO, these defects include vacancies V_{Zn} , VO (missing atoms at regular lattice sites), interstitials Zn_i , O_i (extra atoms occupying interstices in the lattice), and antisites Zn_O and O_{Zn} (Zn atom occupying an O lattice site, or vice versa) [18]. Although intrinsic defects have attracted less attention than metal and non-metal doping, some of these could be electrically, optically, or magnetically active and thus influence ZnO's electrical, optical, and magnetic properties [19]. For example, Zn vacancies rich ZnO exhibited stable *p*-type conductivity over more than two years under ambient conditions [20]. Bandgap reduction due to native defects in ZnO enables a 405 nm laser to sufficiently excite nanoparticles to detect their emissions during live-cell imaging using a confocal microscope, suggesting potential bioimaging

applications [21]. Study on ZnO aqueous suspension has revealed that singly ionized oxygen vacancies facilitated the generation of radical oxygen species (*ROS*) even in the absence of light [22]. Among ZnO native defects, oxygen vacancies have been shown to be beneficial for many applications [23]. Oxygen vacancies rich ZnO obtained by annealing ZnO₂ precursor has been shown more efficient for degradation of 2,4-dichlor-ophenol under visible light irradiation than defect free ZnO [24]. Similarly, ZnO obtained by thermal decomposition of ZnO₂ precursor has been shown much more efficient towards formaldehyde degradation under visible light, than reference obtained by thermal decomposition of Zn(OH)₂ [25]. Ultrathin porous ZnO nanosheets featuring abundant oxygen vacancies were prepared by and successfully tested for dihydroxybenzenes production of phenol under solar light [26]. Recently, Xu et al. reported preparation of surface oxygen vacancy defective black ZnO by high-temperature NaBH₄ reduction, which has been shown to exhibit more than three-times higher solar-driven photocatalytic degradation rate of tetracycline than pristine ZnO [27]. Lv et al. have fabricated ZnO_{1-x} with surface oxygen vacancy by controllable reduction in a H₂ atmosphere and demonstrated its activity for decomposition of methylene blue (*MB*) in solution under *UV* – and visible-light irradiation [28]. Interestingly, they shown, that the bulk oxygen vacancy formed via depth reduction at 700 °C for 5 h resulted in the loss of photoactivity. It is worth mention, that all of these studies utilized either Xe lamp or high pressure mercury lamp, usually in combination with cutoff filter $\lambda \geq 400$ nm.

In this light, synthesis strategies allowing the introduction of native defects in ZnO nanocrystal in a controlled manner are of significant interest. Concerning oxygen vacancies, vacuum deoxidation of ZnO [29] or its annealing a reducing H₂ atmosphere [28] were successfully demonstrated to produce yellowish ZnO with a narrower bandgap value. Thermal decomposition of ZnO precursors, like ZnO₂ [24,25], or Zn(OH)₂ [30] in an air atmosphere has also been reported to redshift the absorption edge and thus promote visible light activity. Other methods reported to be effective in introducing various native defects into metal oxide photocatalysts involve high-energy ball milling [31], laser processing [32], or plasma treatment [33]. Among these, a preparation of oxygen vacancies rich ZnO by the annealing of ZnO₂ appeared to be promising for a large-scale production ZnO with a narrower bandgap. In contrast to modification methods, such as vacuum deoxidation, high energy ball-milling, or annealing in an H₂ reducing atmosphere, which introduce the oxygen vacancies into an existing regular ZnO structure, thermal decomposition of specific precursor produces a defect structure within the whole volume of the ZnO material inherently. In the latter, oxygen vacancies are introduced into the ZnO lattice in a short period in the whole volume of reaction mass during the annealing due to the rapid decomposition of peroxide ions in the course of phase transformation from cubic ZnO₂ phase to hexagonal ZnO phase. Actually, the peroxide decomposition proceeds in each unit cell of the growing ZnO crystal, while the introduction of defects into existing ZnO structure starts from the surface.

Herein, we report on the method of a preparation of ZnO₂ nanocrystals assembly at ambient temperature and pressure, which is easy, low-cost, and potentially suitable for a scaling-up. The annealing of the oxygen-rich ZnO₂ precursor powder at various temperatures yields bandgap-reduced ZnO powder series with variable concentrations of oxygen vacancies. We proposed a photocatalytic experiment for a correct assessment of the photocatalytic activities of samples in the close vicinities of their bandgaps by using monochromatic *LED* irradiation with suitable wavelengths. In contrast to the previous works using intensive polychromatic light sources including some unwanted *UV* radiation, our design enables careful evaluation of the effects of a bandgap narrowing on a visible light photocatalytic activity. Next, we successfully demonstrated the application capability of the prepared bandgap-reduced ZnO for a glass surface functionalization by a simple technique that enables uniform deposition of ZnO₂ nanoparticles easily convertible to its bandgap-reduced ZnO analogs by the annealing of the precursor treated glass surface at the corresponding temperature. The functionalized

glass was shown to be promising in applications that may benefit from the following effects; photocatalytically induced self-cleaning, day-night switchable hydrophilicity/hydrophobicity, and antibacterial effect.

2. Experimental

2.1. Preparation of ZnO₂ precursor and bandgap-reduced ZnO nanocrystals

The pure ZnO powder used as a source and reference material (ZnO-ref) was prepared by zinc oxalate decomposition as described elsewhere [34]. The powdered ZnO₂ precursor was obtained by recrystallization of ZnO-ref dissolved in a mixture of concentrated ammonia and hydrogen peroxide. In brief, 4.2 g of ZnO-ref was added to 350 mL of ammonia solution (25-29%, Penta, Czech Republic) and stirred vigorously for 10 min. Then, 14 mL of H₂O₂ (30% aq., Penta) was added dropwise to the solution, causing ZnO-ref to dissolve quickly. The obtained transparent stock solution was filtered to remove any possible eventual impurities, cast onto Petri dishes of 10 cm diameter. The volume of solution poured into each Petri dish was 20 mL. These solution aliquotes were left for drying in an efficiently ventilated hood due to fast ammonia evaporation, and a dried powder was collected by scratching from the dishes after 2 h. The composition of the powder was confirmed as the desired ZnO₂ precursor. Finally, the ZnO₂ was annealed in a non-ventilated muffle furnace in air atmosphere at various soak temperatures ranging from 200° to 900°C for 2 h. A ramp rate of 10 °C/min was used.

2.2. Preparation of ZnO₂ precursor and bandgap-reduced ZnO functionalized glass

With advantage, we used the stock solution employed previously to prepare ZnO₂ precursor powder and wipe it out directly onto a surface of the etched microscopic glass with dimension 25 × 25 mm using lint-less wipes (Kimtech precise wipes). The thin wet layer dried immediately after wetting, leaving ZnO₂ precursor nanoparticles on the glass surface. Treated glass specimens were annealed at the same heating rate, and temperatures used previously to prepare bandgap-reduced ZnO powders. However, the annealing time was shortened to 15 min due to the limited thermal stability of the microscopic glass. Samples annealed at 700 and 900 °C were excluded from further testing because of defects and deformations due to glass melting.

2.3. Characterization methods

X-ray diffraction analysis was carried out to determine the crystal phase composition of the powdered samples using an X'Pert PRO diffractometer (PANalytical, The Netherlands) equipped with a Cu-K α X-ray tube ($\lambda = 1.5418 \text{ \AA}$) at the operating voltage of 30 kV and the current maintained at 20 mA. Diffractograms were recorded in diffraction angles ranging from 5° to 85° 2θ at the scanning speed of 3°/min. The average crystalline domain size was calculated using the Debye-Scherrer equation $D_c = K\lambda/\beta\cos\theta$, where λ is the Cu-K α line wavelength, β is the peak broadening obtained from the full width at half-maximum (FWHM) intensity of the most prominent (101) diffraction peak in radians corrected by instrumental function, θ is the corresponding diffraction angle, and K factor is 0.9. Morphology of as-prepared samples was observed with the aid of scanning electron microscope Nova-NanoSEM 450 (FEI, The Netherlands). Thermogravimetric analysis (TGA) of the precursor was performed using the thermogravimeter Q500 (TA Instruments, The United States) at a heating rate of

10 °C/min from 25° to 800° C in 30 sccm flowing air. The Raman spectra were recorded in the range of 50-1100 cm⁻¹ by confocal dispersive Raman microscope Alpha300 R + (WITec, Germany) using 532 nm laser with power of 250 μW and 300 Sec exposition. UV-Vis diffuse reflectance spectroscopy (DRUV-Vis) in the range from 265 nm to 800 nm was performed by a modular fiber spectrometer AvaSpec 2048-2 (Avantes, The Netherlands). Belsorp-mini II (BEL Japan, Inc.) apparatus was employed for the specific surface area analysis of all powders, the values were obtained by using the multipoint Brunauer-Emmett-Teller analysis of nitrogen adsorption/desorption isotherms at 77 K. Prior the measurements, the samples were outgassed for 2 h at 80 °C. Electron spin resonance measurements were kindly performed by application scientists at the Bruker BioSpin GmbH site using Bench-Top X-Band CW-EPR Spectrometer System Magnettech ESR5000 (Bruker BioSpin GmbH, Germany). Data were collected under an experimental setup as follows; Microwave power: 1.8 mW, Microwave frequency: 9.43 GHz, Modulation amplitude: 0.2 mT, Modulation frequency: 100 kHz, Time for one scan: 80 Sec, Number of scans: 40, UV source: 100 W Hg arc lamp).

2.4. Evaluation of photocatalytic performance

2.4.1. Evaluation of UV and visible-light photocatalytic activity of bandgap-reduced ZnO powder series

The photocatalytic activity of the prepared materials was evaluated by monitoring the discoloration rate of a Methyl violet 2B (MV 2B) model dye solution at the concentration of 3.5 mg.L⁻¹ under both *UV* and visible light irradiation. For this purpose, we have developed a method that enables to perform a photocatalytic experiment and evaluate the rate of discoloration reaction simultaneously. The photocatalytically-driven degradation is monitored periodically online by a *UV*-Vis spectrophotometer (Varian Carry300). The content of quartz glass cuvette is mixed by a miniature magnetic stirrer while directly irradiated by an exchangeable *LED* of desired wavelength from the top directly in the sample compartment of the spectrometer. The absorption spectra are collected in preselected time intervals which requires the interruption of mixing to allow the catalyst sediment. As the catalyst particles are quite coarse, the clarification of the liquid can be quickly achieved and no spectra deformation due to the suspension turbidity is observed. In all experiments, a photocatalyst load of 10 mg was added to 3 mL of the MV 2B stock solution and stirred in-situ in the cuvette in dark for 1 h to attain adsorption/desorption equilibrium. Afterward, the selected *LED* (Roithner LaserTechnik, Austria) was switched on while further stirring. A spectrum was recorded every 60 min without any need of an additional external measurement. The sample holder in the spectrometer allowed a precise temperature regulation to 25 °C employing Peltier cooler system. The photocatalytic experiments were performed under *UV* light ($\lambda \sim 377$ nm, *FWHM* ~ 15 nm) and visible light ($\lambda \sim 401$ nm, *FWHM* ~ 14 nm, $\lambda \sim 429$ nm, *FWHM* 16 nm) *LED* irradiation. The role of active species involved in the photocatalytic reactions was studied by using disodium ethylenediaminetetraacetate (*EDTA*) and tert-butyl alcohol (*TBA*) as a hole (h⁺) and as a hydroxyl radical scavengers, respectively [35].

2.4.2. Evaluation of the photocatalytic activity of bandgap-reduced ZnO functionalized glass under UV and visible-light irradiation

The photocatalytic activity of bandgap-reduced ZnO nanoparticles on glass surface was evaluated by a photocatalytic test kit Explorer (Ink Intelligent, Belfast, United Kingdom), which is suitable for an assessment of medium active surfaces such as photocatalytic glass, tiles, and similar products. This test kit enables to perform of the photocatalytic experiment according to the ISO 21066:2018 with slight modification [36]. In brief, a defined amount of blue-colored Resazurin based smart ink is applied on the surface of the test-specimens and irradiated with UVA light (UVP-XX-15BLB, 15 W, PN 95-0042-11, Analytik Jena). The light intensity at the surface of the sample was optimized by radiometer RM-22 (Opsytec Dr. Grobel GmbH) to be 2 mW/cm². The color of the film turns into pink during the photocatalytic experiment (for photoactive samples), and the speed of a color change is recorded using a scanner at 5-minute intervals. The time of the color change or even its bleaching is proportional to the sample's photocatalytic activity. The method specified in the ISO 21066:2018 is not dedicated to the assessment of a visible-light activity of photocatalytic surfaces. With the full awareness of possible drawbacks, we developed its analog using a halogen bulb (Gu5.3/MR16, 35 W, Philips) as the visible light irradiation source combined with cut-on filters 395GY50 and 455GY50 (Comar Instruments) of dimensions 50 × 50 mm non-binding. The light intensity on the surface of the sample was optimized to be 2 mW/cm².

2.5. Wettability of bandgap-reduced ZnO functionalized glass

The wettability of bandgap-reduced ZnO functionalized glass samples in response to UV-light exposure was investigated through contact angle measurements on a sessile drop method using SEE System (Advex Instruments, Czech Republic). Five droplets of demi water (conductivity of 0.06 μS.cm⁻¹) of volume 5 μL were placed on the material surface, and the average contact angle was calculated. Measurements were first performed on samples stored in the dark and then after 1 h of irradiation by UV-light (UVP-XX-15BLB, 15 W, PN 95-0042-11, Analytik Jena). After that, samples were restored in the dark and measured at selected intervals for up to 24 h. The measurement was also conducted with the halogen bulb (Gu5.3/MR16, 35 W, Philips) serving as the visible light irradiation source in combination with the cut-on filter 395GY50. The light intensity on the sample surfaces was optimized to be 2 mW/cm² for both UV and visible measurements to keep the same conditions as described in 2.4. The only difference is the application of a single filter in the visible light measurements to mimic the daylight.

2.6. Evaluation of the antibacterial activity of bandgap-reduced ZnO functionalized glass in a dark and under simulated solar light

Testing of the antibacterial activity was performed according to ISO 22196 [37] with modifications. Before antibacterial testing, samples and polypropylene foils were rinsed with 70% denatured ethanol for disinfection. Upon the standard, gram-negative Escherichia coli (CCM 4517) and gram-positive Staphylococcus aureus (CCM 4517) were used. Bacterial suspensions (*E. coli* 4.8 × 10⁵ CFU mL⁻¹; *S. aureus* 2.3 × 10⁵ CFU mL⁻¹) were prepared in 1/500 Nutrient broth (HiMedia Laboratories, India). The size of glass samples was 25 mm × 25 mm. A volume of 100 μL of the bacterial suspension was applied on the modified sample surface, and then it was covered by a polypropylene foil that was square cut previously in size 20 mm x 20 mm. For the control sample, the bacterial suspension was immediately rinsed (i.e., at time 0); the other samples (control and antibacterial treatment) were

divided into two groups. The first group was incubated at 35 °C and 95% RH for 18 h while the samples were simultaneously illuminated from a distance of 30 cm with an artificial daylight source (NARVA LT tube, 36 W/ D65, artificial daylight). The second group of samples was incubated under the same conditions in the dark. Polypropylene foil was removed after the incubation, and each sample was rinsed off entirely with *SCDLP* broth (HiMedia Laboratories, India). The removed liquid was collected and its viable bacterial concentration was determined using the pour plate culture method (PCA, HiMedia Laboratories, India) after incubation at 35 °C for 48 h.

3. Results and discussion

3.1. Bandgap-reduced ZnO powder series study

3.1.1. XRD analysis

The crystalline phase structures of the ZnO-ref, the ZnO₂ precursor, and products obtained by its annealing at various temperatures are shown in a series of diffractograms in **Fig. 1**. The diffractogram of the ZnO₂ precursor material shows broad diffraction peaks at the diffraction angles $2\theta = 31.8^\circ$, 36.9° , 53.2° , and 63.3° , which can be assigned as (111), (200), (220), and (311) planes of the cubic ZnO₂ phase (JCD D PDF-2 entry 01-077-2414), respectively. The slight diffraction peak at the right side, at an angle of $2\theta = 66.5^\circ$, can be indexed to the (222) plane of the same phase. No other phases or impurities were detected. Seemingly, the development of XRD patterns of precursor samples annealed at various temperature follow a typical trend for all inorganics, i.e., narrowing of diffraction peaks and their intensities increasing with an increasing annealing temperature, resulting in an enhancement of coherent scattering domain size and improved crystallinity. Peaks in the XRD pattern of the sample obtained by annealing ZnO₂ precursor at 200 °C can be assigned to the hexagonal wurtzite ZnO phase (JCD D PDF-2 entry 01-079-0207); however, not all crystal planes at higher angles are developed yet. Broad peaks indicate small particle size, with coherent scattering domain size estimated to be around 6.5 nm (for sample ZnO-200) according to the well-known Scherrer formula. The increasing annealing temperature to 300 °C resulted in a slight narrowing of diffraction peaks with a simultaneous increase in signal intensity. Although the triad of peaks at higher angles becomes resolvable, the crystallinity of samples is still rather poor. It can also be observed that poor crystallinity of samples annealed at 200 °C and 300 °C is closely connected with phase transformation reaction from cubic ZnO₂ phase to hexagonal ZnO phase, which involves the rearrangement of octahedrally coordinated Zn(II) to a tetrahedral phase along with the accompanying decomposition of peroxo-ions. The existence of ZnO phase in the poorly crystalline and intermediate state has been substantiated by Daley et al. They directly evidenced this change in the local structure during phase transition in the temperature range from 180° to 250°C through a combined XAS/XRD experiment [38]. On the other hand, intense and narrow diffraction peaks can be observed for the sample annealed at 500 °C, which indicates a significant improvement of crystallinity (note on a different signal intensity scale after a break in **Fig. 1**). The average crystallite size of the coherent scattering domain increased abruptly from the calculated 10 nm for sample ZnO-300-37 nm for sample ZnO-500. Moreover, all crystal planes characteristic for the wurtzite ZnO phase can be identified in the measured range of diffraction angles indicating no preferred particle growth direction. The annealing to 700 °C and 900 °C leads to further coarsening of the particles achieving the average coherent scattering domain size of 56 nm and 67 nm, respectively. A diffractogram of the reference powder ZnO-ref is shown for comparison as well.

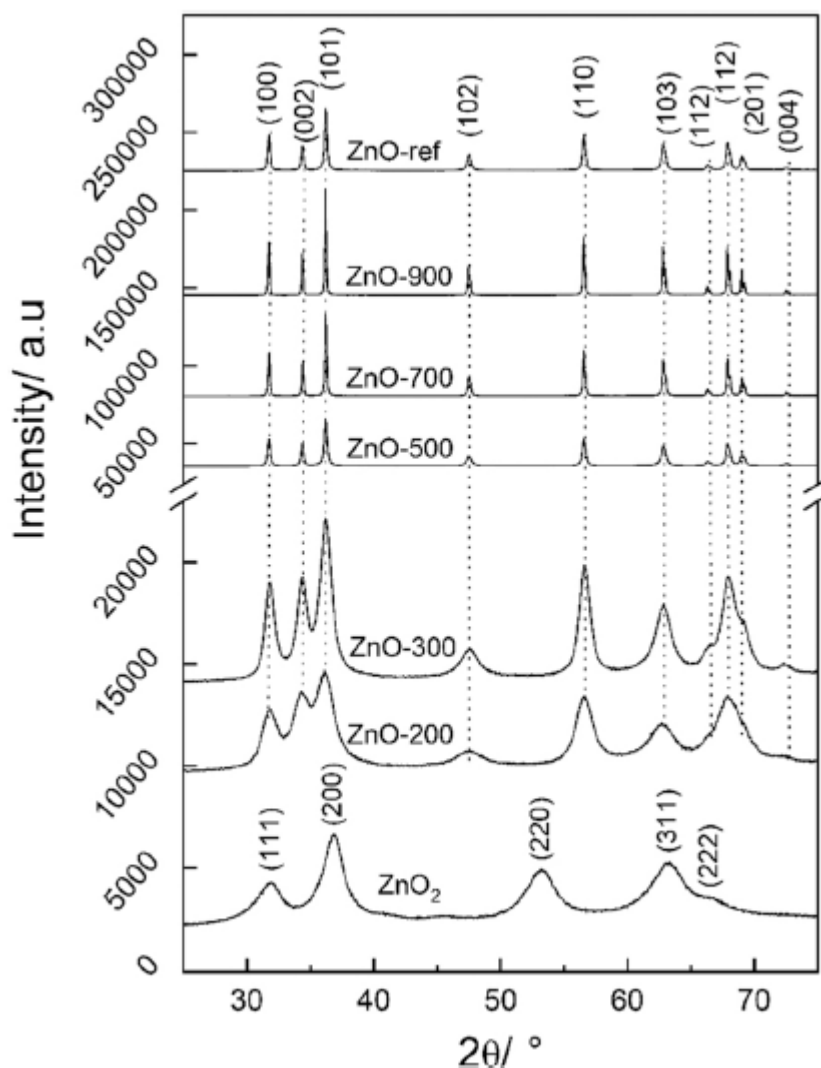


Fig. 1. XRD patterns of powdered samples, including precursor and reference. The labeling of samples corresponds to the annealing temperature.

3.1.2. SEM analysis

The gradual increase in the crystallinity of samples with an increasing annealing temperature corroborates with the morphology evolution as shown by scanning electron microscopy images in **Fig. 2**. The ZnO₂ precursor powder (**Fig. 2a**) consists of well-developed spherical particles with a uniform particle size distribution and an average diameter of about 600 nm. At a closer inspection, these consist of densely packed small crystals assembly with the size of individual crystals being close to the value of coherent crystalline size domain estimated from XRD data. While there is no significant difference in morphologies of precursor material and the sample annealed at 200 °C, the phase transformation from ZnO₂ to ZnO has a noticeable impact on the morphology of the sample annealed at 300 °C, ZnO-300. As can be seen in **Fig. 2c**, the crystals grow and become separated from each other by small voids, and the surface of individual spheres appears rough. This can be attributed to the loss of oxygen over the course of phase transformation and substantial material densification ($\rho_{\text{ZnO}_2}=1.57 \text{ g}\cdot\text{cm}^{-3}$, $\rho_{\text{ZnO}}=5.67 \text{ g}\cdot\text{cm}^{-3}$). The abrupt increase of coherent scattering domain size observed in XRD patterns for the sample annealed at 500 °C is reflected in morphology, which resembles a raspberry-like assembly, as shown in **Fig. 2d**. This effect is more pronounced for the samples annealed at 700 °C and 900 °C, as seen in **Fig. 2e** and **f**, respectively. Various crystal facets of individual crystals can be distinguished.

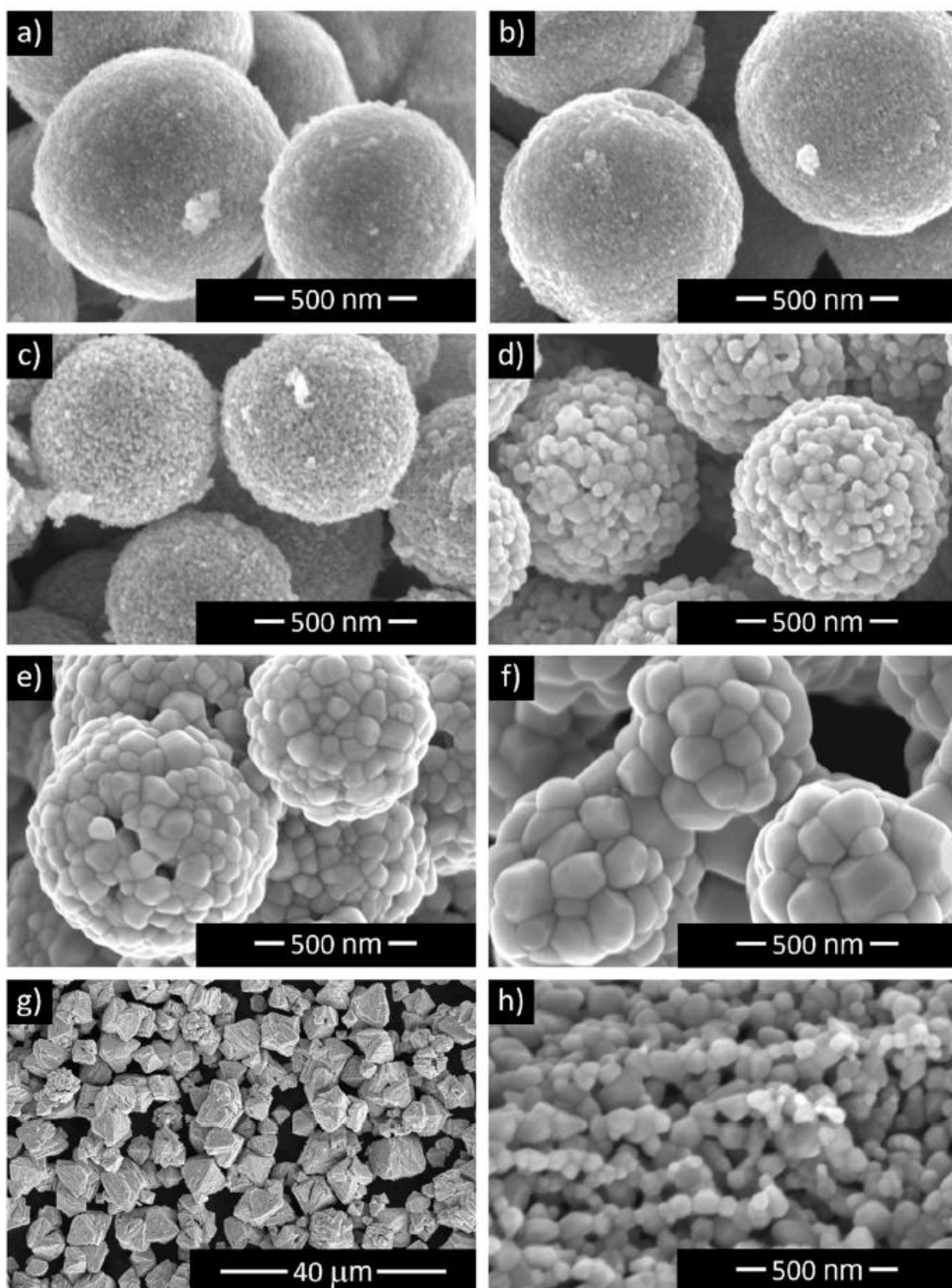


Fig. 2. SEM micrographs of (a) ZnO₂ precursor, and products obtained by annealing; (b) ZnO-200, (c) ZnO-300, (d) ZnO-500, (e) ZnO-700, and (f) ZnO-900. Sample ZnO-ref is shown at low and high resolution in micrographs (g) and (h), respectively.

Moreover, sintering and neck-formation between individual spheres occur as they approach each other at an annealing temperature of 900 °C (**Fig. 2f**). The sintering of individual crystals becomes significant when the annealing temperature is increased to about 500 °C. Above this temperature, the material transport process takes place at a relatively fast rate, driven by the total free energy minimization. Many of highly curved surfaces disappear as the necks form between individual crystals leading to shrinkage and further densification. This trend is well observed in **Fig. 2d-f**, corresponding to the samples annealed at temperatures from 500° to 900°C. The origin of ZnO₂ precursor sphere-like nanocrystals assembly morphology can be found in high ammonia volatility, which causes a rapid decrease in pH and an increase of dissolved species concentration, especially when a large liquid level area is created. After reaching saturation, nucleation occurs within a narrow time interval, as *SEM* shows nanocrystals with uniform size distribution. The sphere-like assembly resulted from surface energy and the minimization of the newly created solid phase in the solution.

3.1.3. TGA analysis

The ZnO₂ precursor decomposes to ZnO with simultaneous evolution of oxygen. **Fig. 3** shows the *TG* curve recorded at a temperature ramp rate of 10 °C/min in synthetic air flow. The mass loss rate (-dTG curve) was obtained by numerical derivation. It is observed that ZnO₂ powder starts to lose weight immediately upon heating, and about 4-5% of initial weight is lost in the temperature region from 25° to 150° C, which is most likely associated with the evaporation of physically bonded water molecules at the ZnO₂ surface. The onset of the decomposition reaction is found above 150 °C with the maximum mass loss rate observed at 221 °C. The decomposition reaction is exothermic, and the decomposition of peroxy- ions induces self-propagating reactions of dioxygen molecule release and peroxide cleavage into oxide(-II) anions. After reaching the temperature of about 250 °C, the termination of the decomposition reaction can be recognized through a break in the TG curve and a sudden decrease in the mass loss rate. Mass loss of ca 13% is recorded between 150 °C and 250 °C. The mass change slowly reaches a plateau at approximately 500 °C. The exact value of the weight loss associated with thermal decomposition can hardly be determined precisely because of moisture presence; however, it can be estimated to 16-17%. This observation is in agreement with values and mechanisms reported elsewhere [39]. TG analysis revealed that phase transformation reaction from the cubic ZnO₂ to the hexagonal ZnO phase occurs mainly in the temperature interval of 150-250 °C. This observation supports the deduction that the poor crystallinity observed in XRD patterns of samples annealed at 200 °C and 300 °C is associated with the quick rearrangement of zinc and oxygen atoms during phase transformation. In comparison, the crystallinity is further improved with the temperature reaching 400-500 °C, which is in good agreement with our *XRD* data as well as with the *DSC* reported in [40].

3.1.4. BET analysis

The specific surface area (*SSA*) is a very important photocatalyst parameter in terms of maximum available surface sites for the photocatalytic reaction. The values of *SSA* are plotted against the annealing temperature in **Fig. 4**. The values of coherent scattering domain sizes estimated according to Scherrer's formula are plotted here for better clarity and comparison.

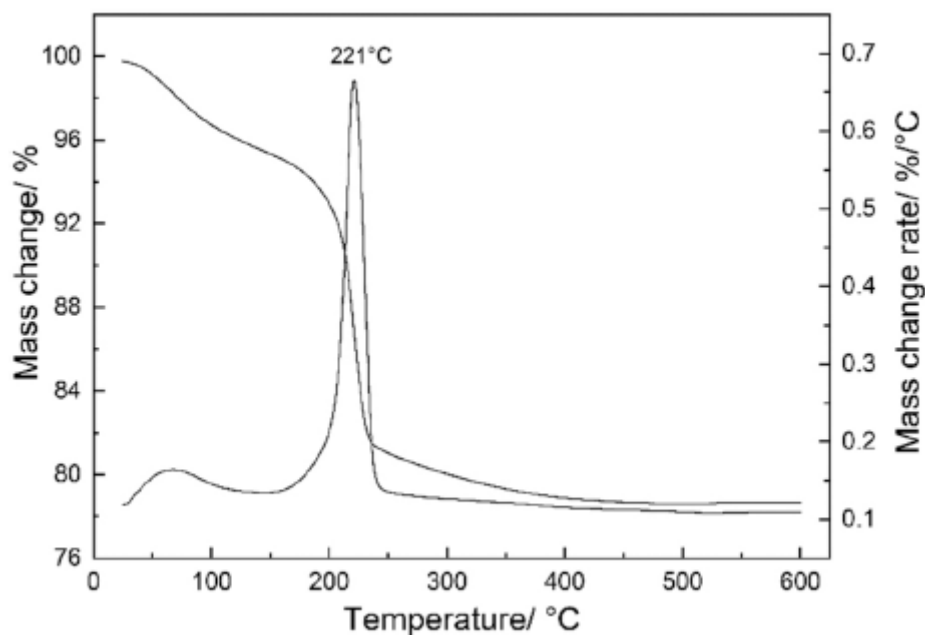


Fig. 3. The *TG* curve of ZnO_2 precursor measured at the temperature ramp rate of $10\text{ }^\circ\text{C}/\text{min}$ in the synthetic air flow, and the corresponding calculated mass loss rate curve.

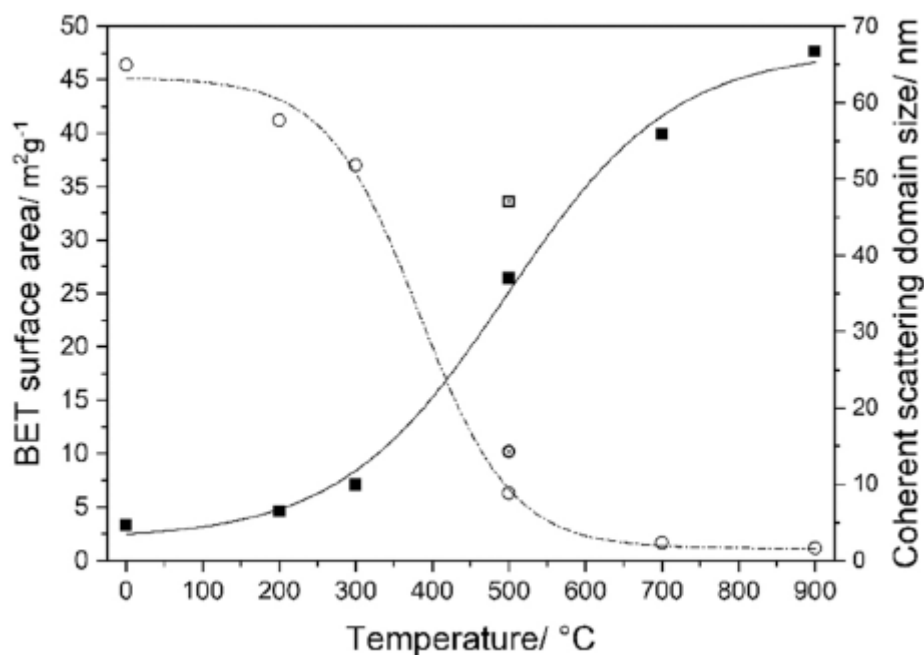


Fig. 4. Dependence of *BET SSA* (empty circles) and coherent scattering domain size (full squares) on the annealing temperature. ZnO-ref is labeled by dotted circle and square for *BET SSA* and coherent scattering domain size, respectively. The scales of y-axes were set to show the two curves in the same proportion as normalized to their saturation or initial point.

It can be seen that the *SSA* data follows a simple sigmoidal decay curve. The precursor ZnO_2 powder possesses *SSA* of about $46\text{ m}^2.\text{g}^{-1}$, which first decreased slowly with increasing annealing temperature, being approximately $37\text{ m}^2.\text{g}^{-1}$ for the sample annealed at $300\text{ }^\circ\text{C}$ and then drops steeply to $6.3\text{ m}^2.\text{g}^{-1}$

for the sample annealed at 500 °C and reaching lowest SSA value, i.e., 1.2 m².g⁻¹ for sample ZnO-900. Precise values of SSA for all samples are given in **Table 1**. Adsorption/desorption isotherms and BJH analysis of pore size distribution can be found in **supplementary information** in Supplement 2 and Supplement 3. A complementary reverse trend is observed for the dependence of coherent scattering domain size (D_c) on temperature. The data follow a simple sigmoidal growth curve with an increasing annealing temperature. The intersection of both curves at approximately 430 °C corresponds to an optimum balance between SSA and D_c . Note that values for SSA and D_c for ZnO-ref obtained by annealing of zinc oxalate under the same conditions as ZnO-500 are shifted towards slightly higher values.

3.1.5. Raman spectroscopy

Raman spectroscopy was further performed to gain thorough insight into the structure of the samples. It can provide useful information about the structure of the samples. It can provide much useful information about structure due to its sensitivity to vibrational, rotational, and other low-frequency modes in a crystal lattice, which are inevitably affected by the incorporation of impurities or native defects. Ramans spectra of ZnO₂ precursor and ZnO powders annealed at various temperatures are displayed in **Fig. 5**.

The spectrum of ZnO₂ precursor is dominated by broadband at frequencies 800-900 cm⁻¹ with a maximum at 839 cm⁻¹, which is related to the O-O stretching vibration of the peroxy- ions. Intense broad bands at the frequency range from 750 to 900 cm⁻¹ are typical for both inorganics and organic peroxides generally [41,42]. The broadband (*) with a maximum at 410 cm⁻¹ should be associated with a lower frequency phonon branch. There are two E₂ modes in the Raman spectrum of ZnO as seen in on the right side of **Fig. 5**; the low-frequency E₂ mode (E₂^{low}) at 98 cm⁻¹, which is related to the vibration of the heavy Zn sub-lattice, and the high-frequency mode (E^{high}) at 437 cm⁻¹ which involves mainly the displacement of the oxygen atoms [43,44]. The intensity of the prominent band at 437 cm⁻¹ of almost all samples increases with increasing annealing temperature, which was confirmed with the ratio of Raman intensities of bands at 437 cm⁻¹ and 333 cm⁻¹ that equals 2.072, 2.374, 1.928, 5.025, 5.307 for samples ZnO-200-900, respectively, and 1.836 for ZnO-ref. It indicates that the oxygen vacancies are more dominant in samples annealed to lower temperatures and their amount decreases with increasing intensity of E₂^{high} [45].

Table 1 BET surface area, crystallite size, the rate constant of dye discoloration for ZnO₂ precursor, and catalytic materials obtained by calcination at various temperatures.

	ZnO-ref	ZnO ₂	ZnO-200	ZnO-300	ZnO-500	ZnO-700	ZnO-900
Coherent scattering domain size ^a [nm]	47	4.7	6.5	10	37	56	67
BET SSA [m ² .g ⁻¹]	10.2	46.4	41.2	37	6.3	1.7	1.2
Bandgap energy E _g [eV]	3.18	– 3.6	3.11	3.08	3.03	3.08	3.16
rate constant [h ⁻¹] (377 nm diode)	54.0 ± 0.7	0.76 ± 0.04	10.8 ± 0.7	7.2 ± 0.1	19.8 ± 0.7	14.4 ± 0.7	20.2 ± 0.3
rate constant [h ⁻¹] (401 nm diode)	25.6 ± 1.1	0.68 ± 0.22	6.8 ± 0.3	8.6 ± 0.3	5.8 ± 0.3	7.2 ± 0.2	5.8 ± 0.3
rate constant [h ⁻¹] (429 nm diode)	0.18 ± 0.01	0.25 ± 0.01	2.12 ± 0.04	2.84 ± 0.07	1.01 ± 0.07	1.69 ± 0.11	0.86 ± 0.11

^a crystallite size was determined according to the Debye-Scherrer equation.

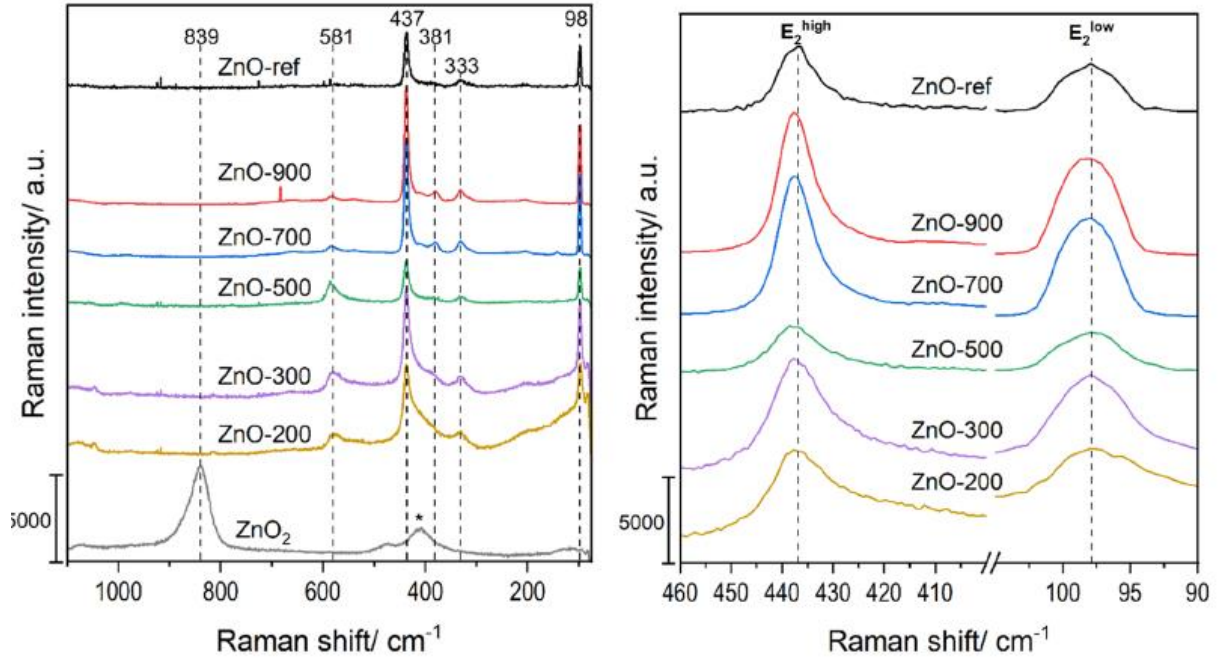


Fig. 5. Raman spectra of all powdered samples (left) and regions of E_2^{high} and E_2^{low} bands of ZnO samples (right).

The sample ZnO-500 is an exception as it evinced a slight decrease of E_2^{high} intensity which indicates a higher amount of oxygen vacancies. This corresponds with yellowish color of the sample, however it does not reflect the difference between ZnO-ref and Zn-500. From this reason, Breit-Wigner-Fano (*BWF*) and phonon confinement models (*PCM*) were further employed to evaluate an influence of the annealing on the Raman bands E_2^{high} and E_2^{low} , whose a/symmetry is evident in **Fig. 5** (right) and characterizes the presence of structural defects in the ZnO sub-lattice. E_2^{high} can be correlated with the amount of oxygen vacancies as it represents the displacement of the oxygen atoms in ZnO sub-lattice as stated above.

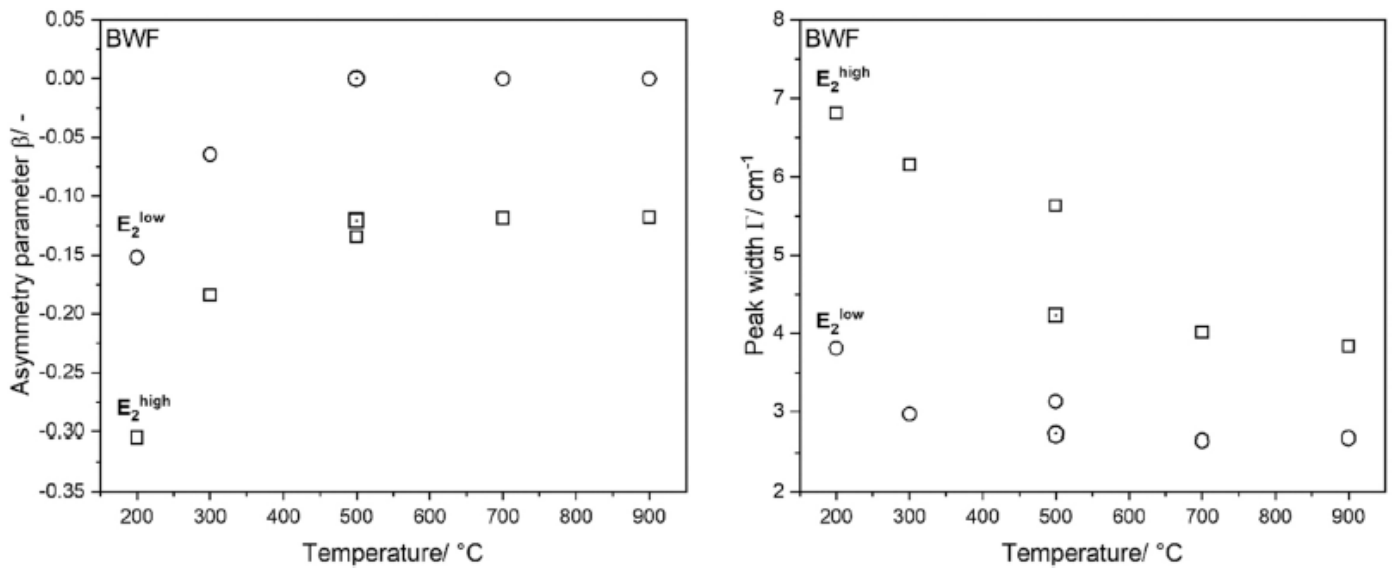


Fig. 6. Evolution of asymmetry parameter β and *BWF* peak width of E_2^{high} (empty squares) and E_2^{low} band (empty circles) with temperature of annealing for ZnO-200-ZnO-900. ZnO-ref is labeled by dotted square and circle accordingly.

BWF model in Eq. (1) describes the Raman intensity $I(\omega)$ (a.u.) with the Raman shift m (cm^{-1}), the *BWF* peak position m_0 (cm^{-1}) at the maximum peak intensity I_0 (a.u.), the half-width at half maximum r (cm^{-1}) and a dimensionless asymmetry parameter β ($= 1/q$) that is a measure of the interaction of the phonon with a continuum of states, i.e. it reflects the ratio between the probability amplitude of the continuum spectra to that of the discrete spectra. As β approaches 0 the Raman mode is more symmetrical [46]. Results of *BWF* fitting and summary of all obtained parameters are given in Supplement 4-6.

$$I(\omega) = I_0 \frac{\left[1 + \frac{(\omega - m_0)}{q\Gamma}\right]^2}{1 + \left[\frac{(\omega - m_0)}{\Gamma}\right]^2} \quad (1)$$

As can be seen in Fig. 6, the asymmetry parameter approaches to zero with the temperature, which confirms that with an increasing annealing temperature the amount of structural defects decreases and corresponds with findings from *XRD* analysis. The presence of oxygen vacancies in ZnO-200 and ZnO-300 can be deduced from the significantly lower symmetry of E_2^{high} connected with oxygen vibrational mode in comparison with E_2^{low} characterized with Zn mode. Moreover, the difference between ZnO-500 and ZnO-ref is now revealed from *BWF* fit of E_2^{high} indicating that ZnO-500 is loaded with higher disorder connected with oxygen displacement. This is seen also from *BWF* peak width dependence on a temperature of the annealing. While ZnO-ref is with the shape and width of the E_2^{high} band close to ZnO-700 and thus more symmetrical, ZnO-500 is clearly closer to ZnO-300, which is significantly less symmetrical and more oxygen vacancies in the structure are expected.

The concentration of defects introduced in the structure of ZnO and a determination of the correlation length representing the dimension where the phonon is not influenced with disorder, is advantageously obtained from *PCM* evaluation of Raman bands. The introduction of defects limits spatial correlation of phonons that has successfully been described by confinement function of Gaussian nature; the correlation function is infinite and Raman spectral line is symmetric and fully Lorentzian only in an ideal crystal [47,48]. Eq. (2) defines the Raman line intensity $I(\omega)$ for the three-dimensional phonon confinement within an isolated nanoscaled sphere ($d^3q \sim q^2 dq$), which is appropriate for objects, such as ZnO powders. Results of *PCM* fitting and summary of all obtained parameters is given in Supplement 6-8.

$$I(\omega) \cong I_0 \int_0^1 \frac{4\pi q^2 \exp\left(-\frac{q^2 L^2}{4}\right)}{[\omega - \omega(q)]^2 + \left[\frac{T_0}{2}\right]^2} dq \quad (2)$$

A term $\exp(-q^2 L^2/4)$ of the equation represents Gaussian spatial correlation function with the correlation length L , which is physically interpreted as an average grain size of a localized region or average size of the material homogeneity region [49,50]. The Raman spectral line shifts toward lower frequencies and the line shape becomes asymmetric with decreasing L [51]. Further, q is the wave vector expressed in the units of $2\pi/\alpha$ (α is lattice parameter), $\omega(q)$ is the function of Raman phonon dispersion relation, and T_0 is the intrinsic Raman line width (*FWHM*). For wurtzite structure of ZnO, $\omega(q)$ is expressed as follows: $\omega(q) = A + B \cos(\pi q)$ where A and B equal 424.5 cm^{-1} and 12.5 cm^{-1} , and 73.8 cm^{-1} and 26 cm^{-1} for E_2^{high} and E_2^{low} mode, respectively. Parameter A is the zone-center phonon frequency, while B is the difference between the zone-center and zone-boundary frequencies of the phonon dispersion curve [52,53]. Fig. 7 shows the dependence of the correlation length and

defect concentration N (nm^{-3}) calculated as $N = 3/(4\pi L^3)$ on the temperature of ZnO annealing. As can be seen, a substantial difference can be found between E_2^{high} ($L = 25\text{-}41$ nm) and E_2^{low} ($L = 15\text{-}21$ nm) modes, and especially in the increasing trend of L vs. temperature of annealing for E_2^{high} . This supports the assumption that a lower temperature of the ZnO annealing encourages the formation of structures with a higher amount of oxygen vacancies. The lower value of L for ZnO-500 in comparison with ZnO-ref indicates a shorter region of phonon distribution without oxygen defects for ZnO-500. An increase of concentration of defects properly correlates with a decrease of the correlation length and the use of a lower temperature of the ZnO annealing, i.e. $N = 0.15\text{-}0.03 \times 10^{-5} \text{ nm}^{-3}$ and $N = 0.76\text{-}0.26 \times 10^{-5} \text{ nm}^{-3}$ for E_2^{high} and E_2^{low} , respectively.

Besides two nonpolar E_2 modes, ZnO possesses according to the theoretical group symmetry, other 10 phonon modes near the center of the Brillouin zone (T), which are represented by the following irreducible representation $T = 2A_1 + 2B_1 + 2E_1 + 2E_2$, where A , B are nondegenerated branches, and E branches are doubly degenerated. The representation follows from the ZnO crystal structure, which belongs to the spatial group $P63mc$ (C_{6v}^4) with two formula units per primitive cell. ZnO possesses a hexagonal lattice, which has two interconnecting sublattices of zinc and oxygen ions, with the Zn^{2+} surrounded by tetrahedral O^{2-} ions and vice versa. The B_1 is a silent mode, the A_1 and E_1 modes are polar and are both Raman and infrared active, whereas the E_2 modes are nonpolar and Raman active only [54]. Accordingly, the weak peaks at frequencies 333 cm^{-1} and 381 cm^{-1} can be assigned to the $(E_2^{\text{high}}) - (-E_2^{\text{low}})$ second-order Raman scattering related to a multi-phonon process and $A_1(TO)$ mode, respectively [39,55]. Intensities of these bands also increased with an increasing annealing temperature, as observed for the Ehigh band at 437 cm^{-1} . The band at frequency of 581 cm^{-1} appeared in the Raman spectra of the annealed samples.

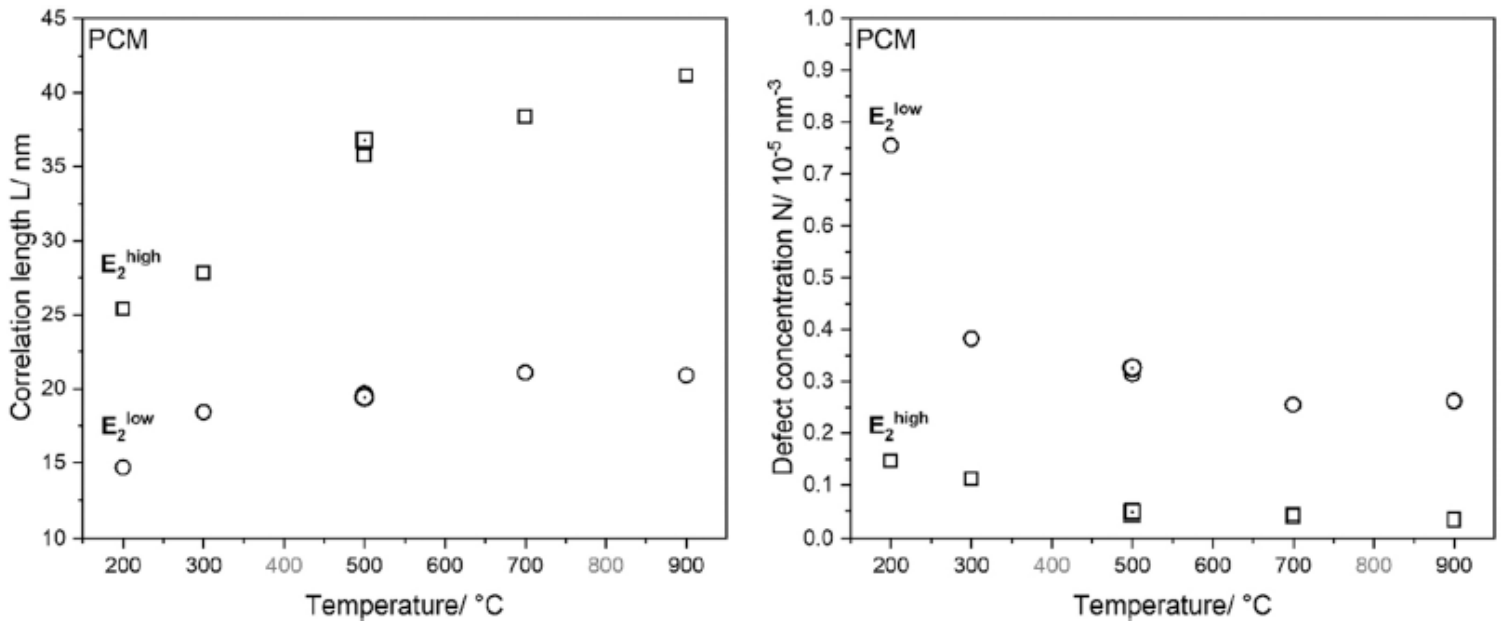


Fig. 7. Correlation length L and defect concentration N of E_2^{high} (empty squares) and E_2^{low} band (empty circles) with temperature of annealing for ZnO-200-ZnO-900. ZnO-ref is labeled by dotted square and circle accordingly.

In contrast to other peaks, whose intensities increase with increasing annealing temperature, the intensity of the band at 581 cm^{-1} reached the maximum value in the case of the sample annealed at $500 \text{ }^\circ\text{C}$ and then gradually decreased as discovered from ratio of corresponding Raman intensities I_{581}/I_{333} that equal to 0.96006, 1.0793, 1.4041, 0.77625, 0.7255 for ZnO-200-ZnO-900, respectively. It should also be noted that this frequency band is missing in the Raman spectra of

reference ZnO powder. The band at frequencies ranging from 550 to 600 cm^{-1} in the Raman spectra of bandgap-reduced ZnO sample series is associated with the presence of oxygen vacancies. Dedicated studies suggest that this band is formed by three peaks sited at frequencies 578, 585, and 590 cm^{-1} , which are associated with the optical phonon $A_1(LO)$ mode, (LO) quasi-mode, and $E_1(LO)$, respectively [30,40,55].

3.1.6. Electron spin resonance measurements

Electron spin resonance is widely employed for studying various defects in ZnO structures, and in fact, it is probably the most successful experimental technique for the identification of native defects in semiconductors. *ESR* spectra for a series of bandgap-reduced powders, precursor, and reference ZnO measured under standard conditions and after 1 h of *UV* light irradiation (Hg arc lamp, 100 W) are plotted in **Fig. 8**. The spectra measured under standard conditions are dominated by a high-field signal corresponding to $g \sim 1.96$, except that of ZnO_2 , which exhibits low-field signals around $g \sim 2.005$. For the bandgap-reduced sample series, the *ESR* signal amplitude at $g \sim 1.96$ increases with an increasing annealing temperature from 200 °C up to 700 °C and then decreases for the sample ZnO-900. Among all samples, a high-field signal amplitude is by far the most intense for samples ZnO-500 and ZnO-700. For a long time, high-field signal at $g \sim 1.96$ has been associated with oxygen vacancies which were believed to be a cause of commonly observed unintentional *n*-type doping [56]. However, recent theoretical and experimental studies indicated that this assignment cannot be correct and that it is actually the signal at $g \sim 1.99$, which corresponds to this kind of native defect in ZnO [57,58] Although V_o has the lowest formation energy among the donor-behaving defects, the *DFT* calculation available in literature indicates that the oxygen vacancy is a very deep donor with an energy level at 1.0 eV below the conduction band rather than a shallow donor, and cannot contribute to the intrinsic *n*-type doping [18]. In principle, the oxygen vacancy in ZnO can exist in three charged states; neutral, + 1, and + 2. Empty oxygen vacancies (V_o^{++}) are potential wells that can trap either one (V_o^+) or two electrons (V_o). Among these defects, it is the unpaired electron of oxygen vacancy in charged state + 1, which is detectable by *ESR*. On the other hand, the theory predicts thermodynamical instability for V_o^+ , which complicates its detection [59]. Consistent with the theory, a metastable oxygen vacancy in V_o^+ charged state can be created by excitation with *UV*-light or electron irradiation [60]. Upon photoexcitation, the *ESR* signal can be detected at low temperatures, but the signal decays with the removing excitation source and increasing temperature. Ischenko et al. concluded that *ESR* signal at $g \sim 1.96$ may be due to one electron weakly bound to ionized impurity atoms [61]. It has been shown that shallow donors doping by group III elements (Al, Ga, In) produces the *ESR* signal at $g \sim 1.96$, which is independent on the doping element and can be enhanced upon *UV*-light irradiation, implying that more electrons have been excited into the conduction band [62].

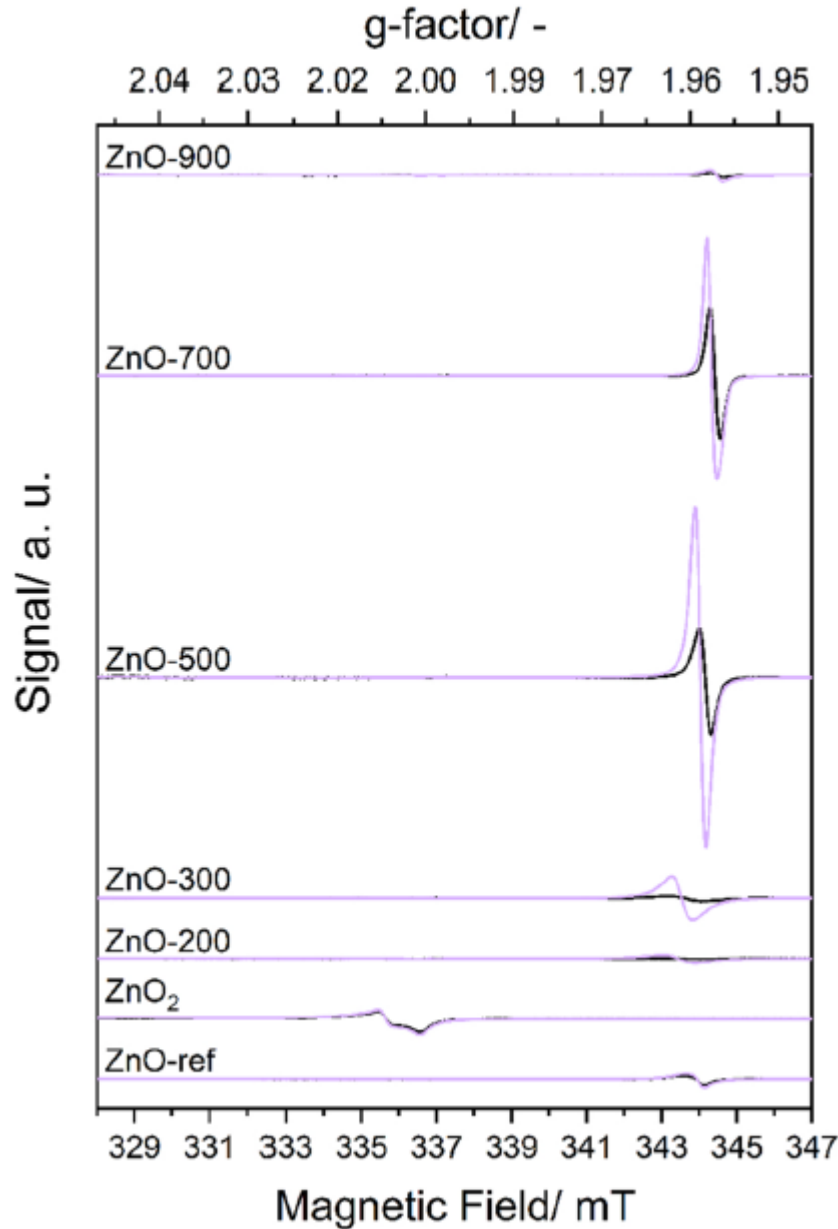


Fig. 8. Electron spin resonance measurements of powdered samples without (black curves) and after 1 h of UV light irradiation (purple curves). Signal intensities are divided 10 times.

On the other hand, there is also strong evidence of studies that ascribed signal at $g \sim 1.96$ to the oxygen vacancies. For example, Halliburton et al. addressed the EPR signal at $g \sim 1.96$ to a contribution of shallow donors and/or conduction-band electrons. Accordingly, if the ground state of V_O is close to the conduction band, an easy thermal promotion of one of two electrons to the conduction band can be expected [63]. Poppl and Volkel estimated the ionization energy for the unpaired electron associated to the signal at $g \sim 1.957$ and found it close to the ionization energy of the ν_{0x} from electrical transport measurements. Such observation points towards a V_O^+ as the responsible source of the signal. The recombination of singly ionized V_O^+ centers does not occur at low temperatures and they are compensated by acceptor-behaving V_{Zn} [64]. Although the oxygen vacancies in ZnO are generally believed of neutral state, a study based on oxygen isotope labeling self-diffusion suggests that they are actually $\nu_{0^{++}}$. Such observation may explain well the generally experienced n-type conductivity as well as the non-stoichiometry of commonly prepared zinc oxide

materials [65]. There are also reports ascribing the low-field signal at $g \sim 2.002$ to the surface located single ionized oxygen vacancies, while the high-field signal at $g \sim 1.96$ originates from bulk species [22,66]. Another aspect, that should be considered here, is the band bending at particle surfaces and/or grain boundaries, which may change in the ionization state of V_o but may also influence the PL intensity of studied material. If the Fermi level (E_F) declines below the V_{o+}/V_{o^+} energy level due to the band bending in depletion region at the particle surface, electrons from all V_{o+} in this region will be emptied, hence all V_{o^x} will turn into $V_{o^{++}}$ and will be diamagnetic. On the other hand, a strong enough illumination may reduce if not fully reverse the band bending due to surface trapping of minority charge carriers which may fill up the VO_{oo} centers by single electrons and convert them to the V_{o^+} state of a paramagnetic nature again [67].

Our observation suggests that oxygen vacancies in paramagnetic V_{o^+} state are inherently incorporated in as-prepared samples ZnO-500 and ZnO-700 in concentration high enough to be detected even without an external source of excitation. Although VO_{oo} are predicted to be not thermodynamically stable, there can be population of oxygen vacancies frozen in high temperature defect equilibrium state, especially when compensated by acceptor-like Zn vacancies, which may eventually also appear during the process of annealing. The decrease of the high-field signal corresponding to $g \sim 1.96$ with an increasing annealing temperature at 900° is in agreement with the theoretical prediction of the migration barrier for V_o^+ and V_o^{++} , which indicated increased mobility and diffusivity above 900 K and 650 K , respectively [56]. After excitation by UV -light, which is, according to literature, one of the common way how to create paramagnetic V_o^+ , intensities of the prominent signal observed at $g \sim 1.96$ increased instead of being detected at a low-field, which suggests that diamagnetic double ionized oxygen vacancies VO_{oo} are converted to VO_o state by trapping photoexcited electron. The effect of UV -light irradiation on high-field signal intensity is most pronounced for samples ZnO-500 and ZnO-700, which yield the most intense signals among bandgap-reduced ZnO powder series without excitation. More detailed visualization of signal amplitude plotted as a function of irradiation time can be found in Supplement 9.

The ESR spectrum of ZnO_2 precursor, which exhibits low-field signals around values of $g \sim 2.005$, is in agreement with spectra reported elsewhere [68]. Besides ZnO_2 , high-field signals, although of very low intensities, were detected for all samples except ZnO-300, ZnO-500, and ZnO-700, which exhibit low-field signal only (see full-size image ESR single spectra at the high resolution provided in Supplement 10). In fact, the spectrum of V_o^+ is composed from two independent contributing signals; a broader low-field signal component which has no photoresponse, and a sharper strongly photosensitive high-field signal component. Apart from halogen substitution of oxygen, which is improbable in our case, the low-field signal can be associated with a pair of V_o and O_i . The high-field signal is interpreted as a manifestation purely of an isolated paramagnetic V^+ [69]. Nevertheless, the absence of a low-field signal for samples annealed at $300, 500, \text{ and } 700^\circ\text{C}$ should also indicate oxygen vacancies prevailing in bulk, while the low-field signal observed in spectra for the low and high annealing temperature, ZnO-200 and ZnO-900, testifies for surface defects.

3.1.7. Optical properties

As can be seen in Fig. 9, the presence of oxygen vacancies in bandgap-reduced ZnO powder series also influenced optical properties. A series of powder images at the top of Fig. 9 evidently illustrates the gradual color change from white to yellow with an increasing annealing temperature up to 500°C and then back to white with a tinge of green color. Especially the yellowish color of the sample obtained by annealing of ZnO_2 at 500°C is in the contrast with the white reference sample obtained by an

annealing of zinc oxalate precursor at the same temperature. A similar trend was reported in [24,25]. ZnO itself is thermochromic material, and it changes color from white to pale yellow when heated in an oxidative atmosphere but turns back to snow-white after cooling down. Generally, this color change is attributed to temporary substoichiometry of oxygen in ZnO at high temperatures. Thus, even this simple evidence of powder series color by the naked eye indicates the presence of oxygen vacancies, which are most likely frozen in high temperature metastable thermodynamic state after cooling. Diffuse reflectance spectra of the bandgap-reduced ZnO samples series, ZnO₂ precursor, and reference ZnO are shown in right panel in **Fig. 9**.

Zinc peroxide is a wide bandgap semiconductor with an absorption edge of about 350 nm. The absorption edge of the reference ZnO powder is also in the UV light region but shifted to wavelengths around 390 nm. The absorption edge of bandgap-reduced ZnO sample series first red-shifts with an increasing annealing temperature up to 500 °C due to the introduction of oxygen vacancies, and then blueshifts again as oxygen vacancies diffuse out with a further increase of the temperature. In fact, the variation of slope in diffuse reflectance spectra observed for the bandgap-reduced sample series is a typical manifestation of various states in the forbidden band. A sharp drop in the reflectance is more reminiscent of a sharp excitonic transition just below the band edge, whereas a slow drop-off is indicative of a whole band being involved [70]. It should be noted that these changes in slope also correlate with the change in intensity of high-field signal observed in *ESR* spectra for bandgap-reduced ZnO powder series. The direct optical bandgap energies of the prepared samples were also estimated from Tauc plots, as shown in the right panel in **Fig. 9**. The highest calculated optical bandgap values for ZnO-ref and Zn-900 °C were 3.18 eV and 3.16 eV, respectively, while the minimum optical bandgap energy of 3.03 eV was calculated for the sample annealed at 500 °C. This implies that the synthesis method directly affected the optical properties resulting in the narrowing of the bandgap, which should be desirable in photocatalytic materials. The high concentration of oxygen vacancies in resulting product is a characteristic of the given precursor and is related to the release of peroxy-ions during the thermal decomposition of ZnO₂. To complete the bandgap analysis, the E_g of ZnO₂ may be estimated at ~ 3.6 eV. The E_g values for all samples are listed in **Table 1**.

Photoluminescence (*PL*) spectra were measured to provide further insight into the optical properties of the prepared bandgap-reduced ZnO powder series. The typical *PL* spectrum of ZnO comprises of a relatively sharp band-gap emission in the UVA region and a broad emission band in the visible region related to various usually surface native defects and metal ions impurities [71,72]. As can be seen in **Fig. 10**, ZnO-ref exhibits an intense emission at 385 nm, originating from the radiative recombination of free excitons near the band edge [73]. Qualitatively judging, the intensity of this peak for bandgap-reduced sample series first decreases with annealing up to 500 °C and then increases again in the same trend as observed in diffuse reflectance spectra and the *ESR* measurements. However, the *PL* data quality in this region do not allow unambiguous deconvolution and quantitative analysis of the peak intensity, position and width changes to corroborate the results thoroughly. Moreover, deep-level green emission appears in the spectrum recorded for sample ZnO-900, usually attributed to surface oxygen vacancies [69].

The absence of emission in visible light for other samples can be explained by the adsorption of various molecules from a surrounding environment during *PL* measurements. It was shown in the literature that inert (N_2) and reactive (O_2) molecules could be adsorbed on the surface of ZnO and induce charge transfer (*CT*). The band emission is significantly quenched by non-radiative N_2 *CT* states, while the *CT* states generated by adsorption of dioxygen molecules recombine radiatively in a visible light region, increasing thus the overall *PL* quantum yield [74].

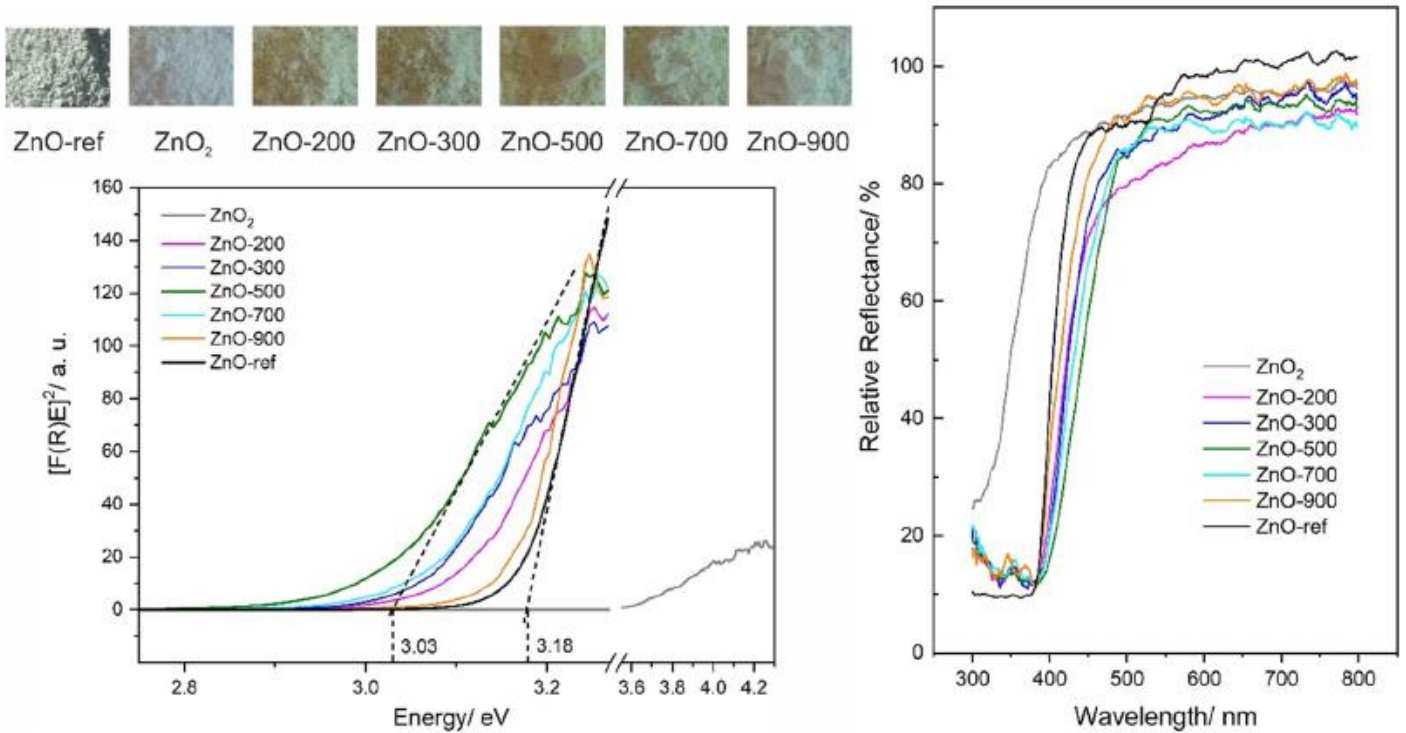


Fig. 9. Bandgap energies (left panel), UV-Vis diffuse reflectance spectra (right panel), and photo images of powdered samples.

Similarly, Djurisić et al. observed that green luminescence is significantly reduced after coating ZnO with a thin layer of surfactant, suggesting that a major part of green luminescence is related to surface defects [75]. Although the correlation between *PL* spectra and photocatalytic activity is not clearly proved yet; nonetheless, *PL* spectra can provide important insight into crystal characteristics such as surface defects, oxygen vacancies, surface states, photo-induced charge carrier separation, and recombination processes in nano-sized semiconductor materials [76]. There is an ongoing scientific discussion regarding the effect of *PL* on photocatalytic activity. One scientific group holds the view that an increase in *PL* intensity positively affects the activity of semiconductor photocatalysts. An improvement of the photocatalytic activity is usually ascribed simply to the enhanced charge carrier separation, which in turn results in an increase in overall quantum yield of the photocatalytic reaction. On the contrary, it is also accepted in the scientific community that a lower *PL* intensity results in efficient charge carrier separation. The lower *PL* signal intensities of colored powders are likely related to the defects responsible for the absorption of visible light. These defects act as recombination centers.

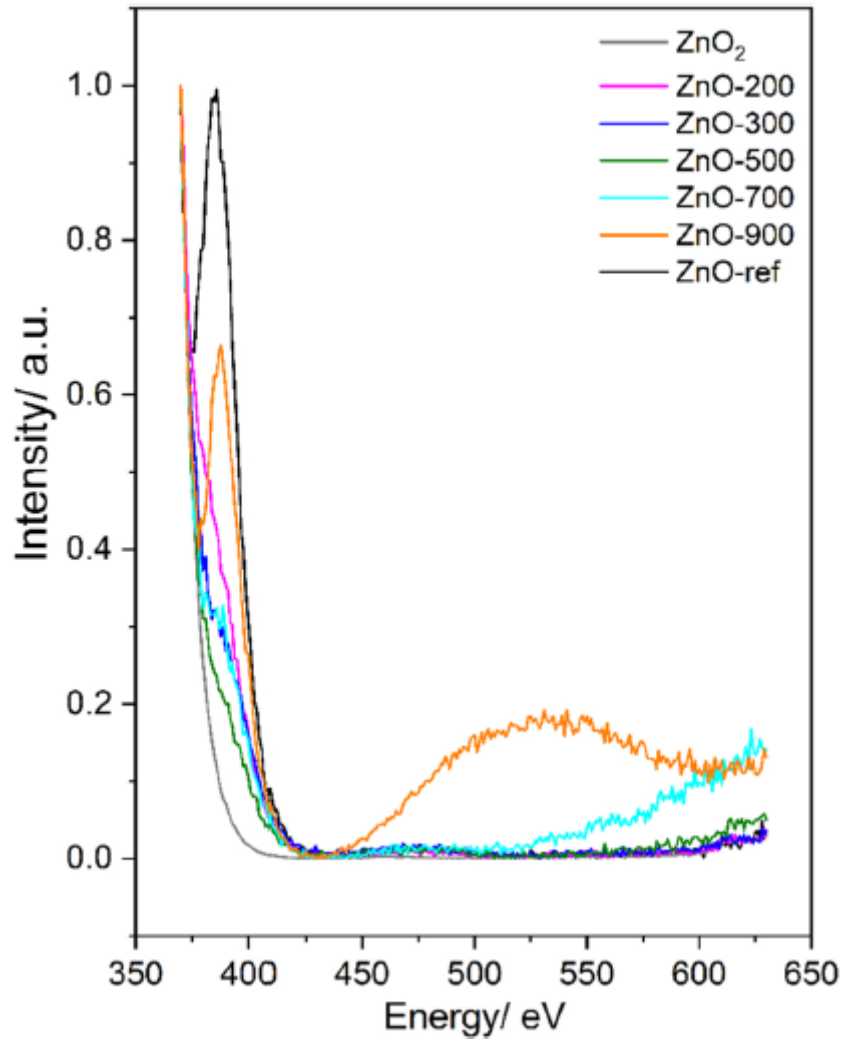


Fig. 10. Photoluminescence spectra of prepared powders obtained by laser with excitation wavelength $\lambda = 331$ nm.

It should be hypothesized based on the analysis of the dataset obtained using complementary instrumental techniques that oxygen vacancies are introduced into the crystal lattice of ZnO during phase transformation from ZnO₂ to ZnO, which is connected with a rapid decomposition of peroxo-ions in a narrow time interval and whole mass of powder. The release of dioxygen leaves oxygen vacancies in the structure. Their concentration varies with the annealing temperature, with a maximum for the sample ZnO-500. The decrease observed for samples prepared at higher temperatures is due to increased mobility and diffusivity of vacancies at high temperatures. At the same time, the concentration profile of oxygen vacancies varies from bulk to surface (with bulk oxygen vacancies being dominant from 300 up to 700 °C), and also the ratio between oxygen vacancies with various formation energy, mainly V_0^+ and V_0^{++} frozen in high temperature metastable thermodynamic state could be affected due to variation of depleted diamagnetic layer thickness.

3.1.8. Evaluation of UV and visible-light photocatalytic activity

Photocatalytic activity of powdered series of bandgap-reduced ZnO was evaluated by means of monitoring the discoloration rate of Methyl Violet 2B solution under both UV and visible light

irradiation. The vast majority of available reports on visible light photocatalytic activity referring to photocatalytic experiments were carried out simply under fluorescent lamp irradiation in combination with a *UV* cut-off filter. In contrast, we used a cuvette holder housing equipped with the *LED* mounted directly in-situ of the spectrometer as an irradiation source. The cuvette itself serves as a miniature photocatalytic reactor in this setup. One particular advantage such a setup provides is that the degradation reaction of a model pollutant can be monitored online during the photocatalytic experiment without the need for sampling. Diodes can be easily changed, enabling photocatalytic activities of samples to be examined closely to the estimated bandgaps ($E_g = 3.03$ eV for sample ZnO-500, corresponding to the wavelength of 409 nm; $E_g = 3.18$ eV for sample ZnO-ref, corresponding to the wavelength with maxima at 390 nm) by using diodes emitting at 377 nm, 401 nm, and 429 nm wavelengths as illustrated in **Fig. 11**.

The results of photocatalytic experiments expressed as rate constants are summarized in **Table 1**. Interestingly, the ZnO-500 powder with E_g 3.03 eV (corresponding to the wavelength 409 nm) exhibits worth photocatalytic performance under *LED* with maxima at 401 nm than the ZnO-ref sample with bandgap value $E_g = 3.18$ eV (corresponding to wavelength 390 nm), which can be ascribed to a broad distribution of intensities of *LED* source with *FWHM* ~ 15 nm. The photocatalytic activity for bandgap-reduced ZnO is relatively small under irradiation by 429 nm diode, which can be expected as photons with energy 3.03 eV (corresponding to sample ZnO-500 with most reduced bandgap) or higher are required for photoexcitation of e^-/h^+ pairs, and the diode with maxima at 429 nm (2.91 eV) possesses insufficient energy potential to do so. However, the ZnO-300 and ZnO-500 exhibit visible-light (under *LED* with wavelength maxima at 429 nm) photocatalytic activity better than ZnO-ref due to their ability to trap photo-excited electrons by singly or doubly ionized oxygen vacancies below its conduction band. For the graphs of normalized concentrations (represented by the natural log of C_0/C_t , where C_0 and C_t are the concentration of MV 2B) at reaction time t , see Supplements **11-13**. It is also observed that the *SSA* does not play a significant role in photocatalytic activity, and no positive correlation was noticed. In fact, *SSA* decreases steeply from 37 for the sample ZnO-300-6.3 m^2g^{-1} for the sample ZnO-500 which is accompanied by losing porosity because of sintering and growth of individual grains (see Supplement 3 - BJH plot). Nevertheless, the effect of a specific surface, which shall otherwise be beneficial for photocatalysis, is at the expense of improperly developed ZnO crystalline phase and coherent scattering domain.

Therefore, it can be inferred that the contribution of modified ZnO samples towards photocatalytic activity is solely due to factors influencing optical properties. Several authors have attributed an enhanced photocatalytic activity in the visible light range to the oxygen vacancies induced bandgap narrowing caused by an increased amount of oxygen vacancies [24,77]. Nevertheless, our results suggest somewhat limited performance in the visible-light region as the bandgap narrowing is mainly due to the intra-band state of singly or doubly ionized oxygen vacancies, which act as electron traps as suggested by *ESR* and *PL* measurements. This could also explain the lower photocatalytic activity of oxygen vacancy-rich samples compared to defect-free ZnO-ref with structural parameters close to that of sample ZnO-500, including average coherent scattering domain size and *SSA*. In order to investigate prevailing mode of photocatalytic driven reaction, photocatalytic experiments were repeated in the presence of scavengers under *LED* with maxima wavelength at 377 and 401 nm (see Supplements **14** and **15**) for samples ZnO-ref and ZnO-500. *EDTA* was used to selectively block holes, h^+ , while *TBA* reacts preferentially with excited electrons and/or hydroxyl groups intermediate [78]. It was observed that neither *EDTA* nor *TBA* increased photocatalytic activity of ZnO at all under 377 nm *LED* irradiation. Photocatalytic activity of sample ZnO-ref is slightly lowered in the presence of *TBA*, but *EDTA* inhibits significantly photocatalytic driven discoloration reaction by a killing of effectively

photogenerated holes. Although the mechanism of photocatalytic action is not so straightforward, holes are believed to be dominant reactive species oxidizing water molecules [79].

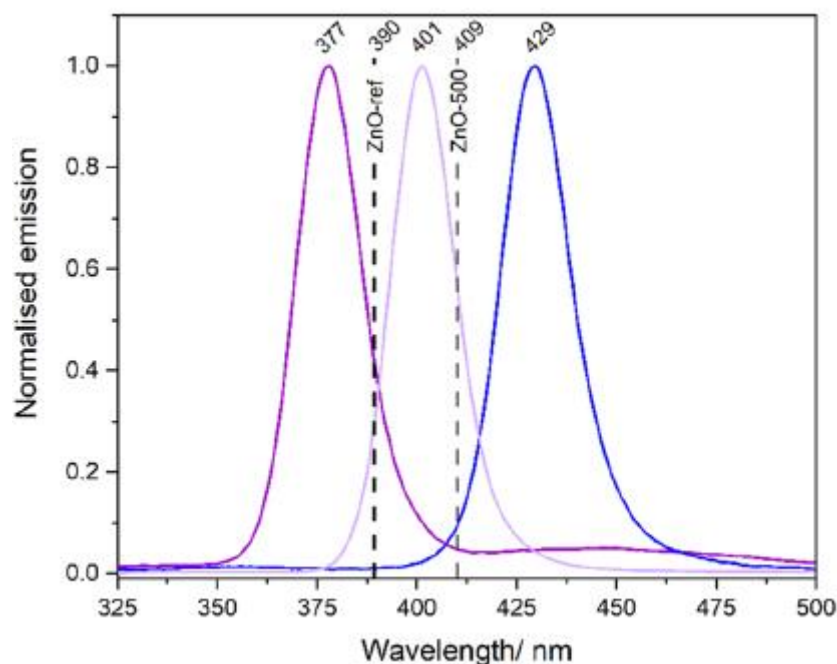


Fig. 11. Maxima wavelength of LED used for irradiation of powdered samples ($\lambda = 377, 401, 429$ nm). Dashed lines at 390 and 409 nm correspond to bandgap energies of ZnO-ref and ZnO-500, respectively.

The mechanism is much more complicated for the sample ZnO-500. In presence of scavengers, the photocatalytic activity is halved irrespectively of scavenger used, which indicates a balanced effect of oxidizing holes and reducing electrons. Such photocatalyst has enormous potential since both oxidative and reductive reaction pathways are active maximizing thus the efficiency of the process. However, it is impossible to make any specific conclusion from the scavenger experiment under 401 nm LED irradiation. Photocatalytic performance is rather low even without the addition of scavengers, and if added even lowered approximately to the same level irrespectively on scavenger. Again here, the balanced effect of scavengers might indicate the presence of both reaction pathways, but the effects are not significant enough.

3.2. Bandgap-reduced ZnO functionalized glass study

3.2.1. Glass functionalization and SEM analysis

After complete characterization of as prepared bandgap-reduced ZnO nanocrystals assembly in a powder form, we tried to transfer these particles onto a glass substrate with the aim to impart its surface photocatalytic, self-cleaning, and antibacterial properties. For this purpose, we have used etched microscopic glass cut to 25 × 25 mm dimensions. Morphology of the etched surface of a glass substrate is shown in **Fig. 12a, b** at low and high magnification. Precursor ZnO₂ nanoparticles can be deposited onto a glass surface easily from the stock solution used previously for the preparation of precursor in powder form, as illustrated in **Fig. 12c**. Ammonia in a thin layer of stock solution evaporates almost immediately after deposition inducing fast crystallization of ZnO₂ nanoparticles densely packed in a thin uniform layer covering the glass surface.

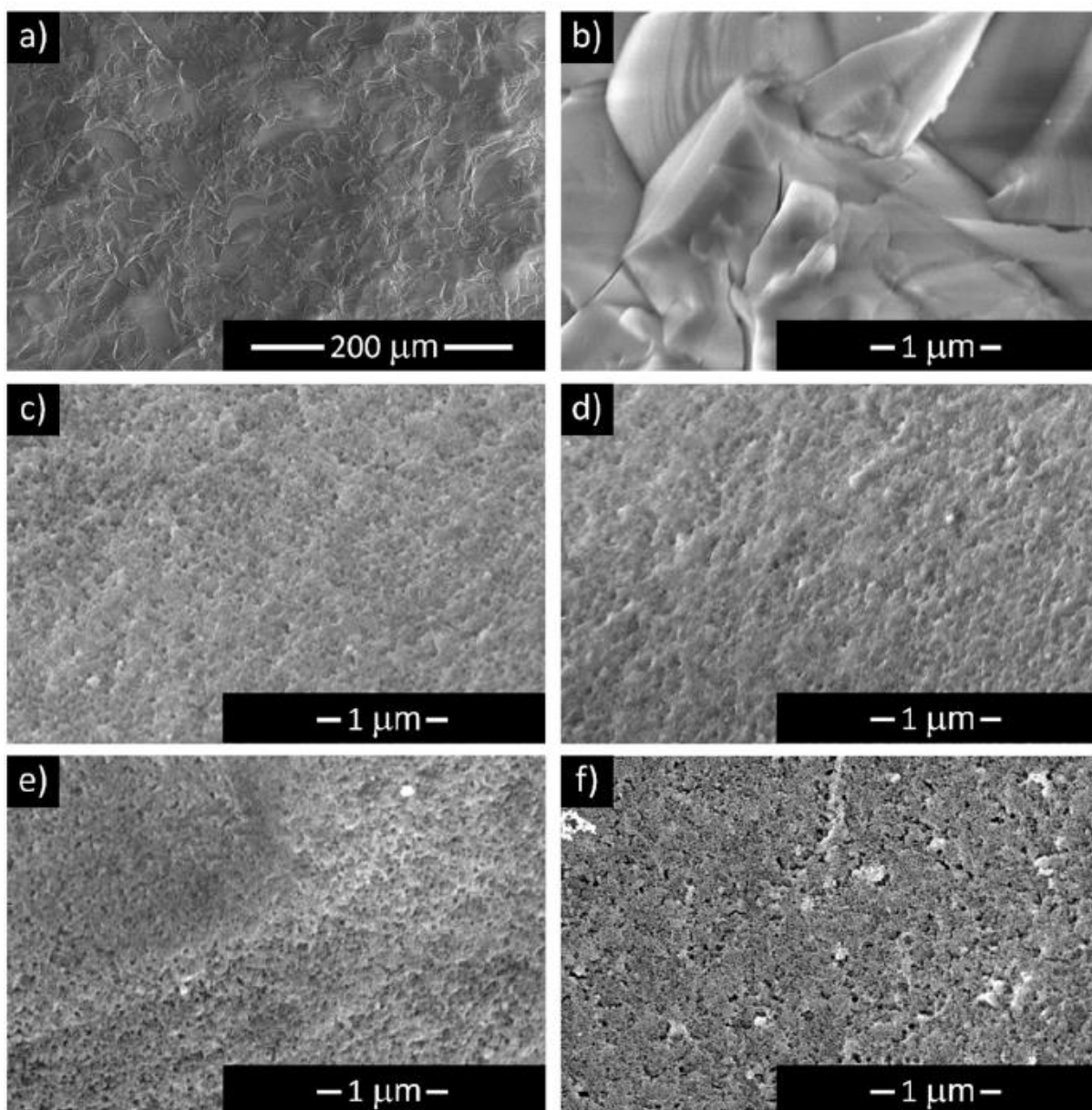
































Fig. 12. Scanning electron micrographs of the etched surface of the glass substrate at low and high magnification (a,b) surface treated by ZnO₂ (c), and bandgap-reduced ZnO treated surface ZnO-200 (d), ZnO-300 (e), and ZnO-500 (f).

Morphologies of the ZnO₂ precursor nanoparticles covered glass after conversion to bandgap-reduced ZnO treated glass by annealing at 200, 300, and 500 ° C are shown in **Fig. 12d-f**. The morphology of the sample annealed at 200 ° C is somewhat amorphous-like in comparison to both the precursor and product at 300 ° C invoking an intermediate stage between decomposition of the original precursor crystallites and reassembly of the new phase particles (**Fig. 12d**). Indeed, the poor crystallinity of samples annealed at 200 ° C was already noticed at *XRD* characterization of powdered samples and is closely connected with the phase transformation from cubic ZnO₂ phase to hexagonal ZnO phase, which accompanies the rearrangement of octahedrally coordinated Zn(II) to tetrahedrally coordinated Zn(II) along with the release of peroxy-ions at the temperatures ranging from 150° to 250°C.

The crystallinity of bandgap-reduced ZnO increased after passing this intermediate state by annealing at 300 ° C, and individual nanoparticles became apparent, as documented in **Fig. 12e**. The sample treated at 500 ° C, which corresponds to bandgap-reduced ZnO powder with the highest concentration

of oxygen vacancies, is crystalline with particles of sharp edges observed in secondary electron mode, and the presence of voids indicates initial nanoparticles coalescence and sintering. After confirmation of successful deposition of ZnO₂ precursor and bandgap-reduced ZnO nanoparticles on the glass surface by *SEM*, testing of functional properties proceeded without further characterization, which was done earlier on powder analogs.

Table 2 Series of images of Resazurin based ink motif layer onto glass surface before (0 min) and after the photocatalytic experiment (60 min) under *UV*-light (365 nm) and visible-light irradiation with cut-on filters (395 and 455 nm).

Irradiation source: UV-light (365 nm)					
Irradiation time [min]	blank glass	ZnO ₂	ZnO-200	ZnO-300	ZnO-500
0					
60					
Irradiation source: Visible-light source with cut-on filter (395 nm)					
Irradiation time [min]	blank glass	ZnO ₂	ZnO-200	ZnO-300	ZnO-500
0					
60					
Irradiation source: Visible-light source with cut-on filter (455 nm)					
Irradiation time [min]	blank glass	ZnO ₂	ZnO-200	ZnO-300	ZnO-500
0					
60					

3.2.2. Evaluation of *UV* and visible-light photocatalytic activity

In the first, the photocatalytic activity of the functionalized glass was evaluated with the photocatalytic test kit according to the ISO 21066:2018. Results of photocatalytic tests for a blank glass substrate, ZnO₂ precursor, and bandgap-reduced ZnO treated glass samples under *UV*-light irradiation are visualized in the first two rows in **Table 2**. The appearance of the motif sketched onto the surface of either functionalized or blank glass substrate by photocatalytic pen was blue at the beginning of the

experiment, i.e. irradiation time is 0 min (first row, **Table 2**). The photocatalytic test was terminated after 60 min of UV-light irradiation as recommended, and the results are shown in the second row in **Table 2**. It can be seen that ink color did not change upon 60 min of UV-light irradiation in the absence of photocatalyst, i.e., when sketched on the blank glass substrate and the same hold for ZnO₂ precursor treated glass and even for the sample annealed at 200 °C.

In contrast, the ink changed color from blue to pink after 60 min of UV-light irradiation for samples ZnO-300 and ZnO-500 indicating significant photocatalytic activities. This color change of the photocatalytic active ink is based on the irreversible reduction of Resazurin (*Rz*) to Resofurin (*Rf*) by photogenerated electrons and/or electron-mediated ROS and can be detected in a UV-Vis spectrum by changes of absorbance at 609 nm (decreases due to the reduction of *Rz*) and 582 nm (increases due to the production of *Rf*) [80]. Besides reductive dye, the ink comprises glycerol as a sacrificial electron donor killing effectively photogenerated holes, and hydroxyethylcellulose as a thickening agent facilitating electron transfer [81]. It should be mentioned that **Table 2** shows initial and final scans only, but the color change takes place almost immediately after five minutes of irradiation for samples ZnO-300 and ZnO-500 and then the motif slowly bleached. Bleaching is attributed to the conversion of *Rf* to dihydro-resorufin (*DH – Rf*), which is slow compared to the rapid initial change of color from blue to pink due to the reduction of *Rz* to *Rf* [82]. For the complete series of images scanned in 5 min intervals, see Supplements 16, 17, and 18. The absence of photocatalytic activity for the sample annealed at 200 °C can be explained by its prevailing hole dependent mechanism (killed by the present glycerol scavenger) as the analogous powdered sample exhibit moderate photocatalytic activity towards MV 2B discoloration in solution.

Although it is not recommended in ISO 21066:2018 to perform the photocatalytic test under visible light, we have tried it with precaution. Testing of the photocatalytic activity, based on monitoring the discoloration rate of dyes, is always disputable due to possible dye sensitization and/or photodegradation encountered inevitably in the visible light [83,84]. On the other hand, testing of the photocatalytic activity under visible light irradiation by using the *Rz* based photocatalytic ink has been already reported yet on pressed powdered samples, and it was shown that *Rz* bleached only slowly under LED irradiations with maxima of wavelength at 617 nm and that a rate is largely independent of the semiconductor used, suggesting dye degradation via photolysis rather than dye sensitization [85]. Nevertheless, we first applied a visible light irradiation source (see relative spectral distribution in **Fig. 13**) in combination with the cut-on filter passing light of the wavelength of 455 nm (corresponding to energy 2.73 eV) and longer in order to evaluate the contribution of dye bleaching since the energy of passing light is not enough for photoexcitation of the bandgap-reduced ZnO.

As can be seen in the middle two rows in **Table 2**, the smart ink is not sensitive enough to detect any change in the color of motif layers suggesting the contribution of photolysis to be negligible. After this finding, we repeated the experiment with a cut-on filter passing light of wavelengths longer than 395 nm. This wavelength corresponds to the energy of 3.14 eV, which means that at least ZnO-500 sample with bandgap 3.03 eV (corresponding to wavelength 409 nm) can respond under the given experimental setup. At the same time, photoexcitation of bandgap-reduced ZnO is limited to the visible

light spectrum by effective filtering of *UV*-light (only light above 395 nm passed), which can be a source of false-positive results although being of very low intensities.

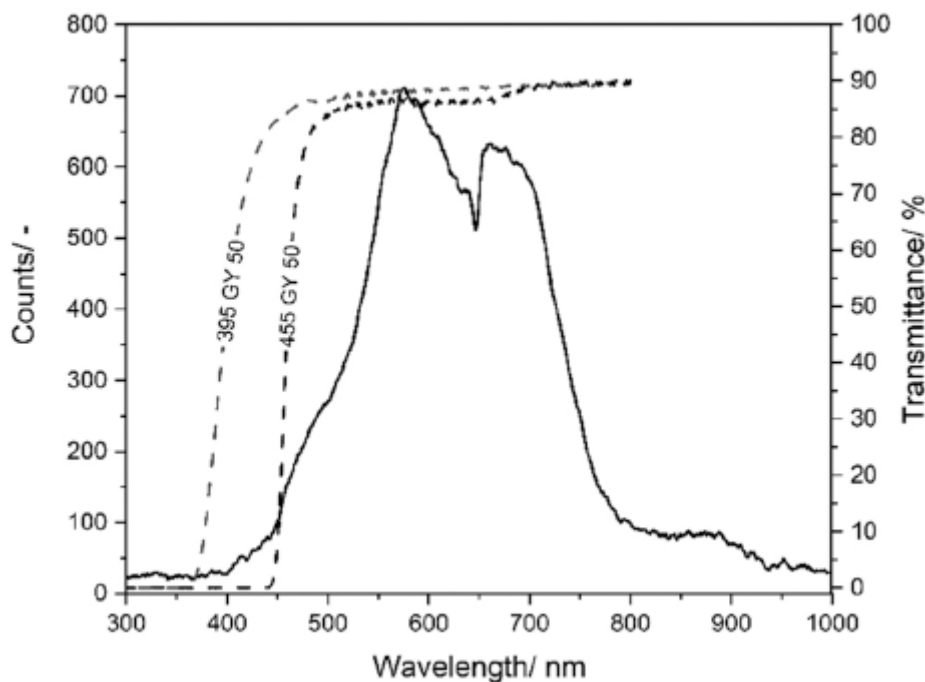


Fig. 13. Relative spectral distribution of the visible-light source (Gu5.3/MR16, 35 W, Philips) with cut-on filters passing light above 395 nm (GY395, Comar Instruments) and 455 nm (GY455, Comar Instruments). Measurements were done at a distance where the intensity was 1000 lux with 100 detector integration time.

However, a series of images in two rows at the bottom in **Table 2** clearly show that there are no changes of color of the motif layer suggesting thus no or negligible photocatalytic activity. These results are in contrast with expectations based on a favorable alignment of energies of bandgap-reduced ZnO and energies of photons of passed light which seems to be sufficient for its photoexcitation. Lack of photocatalytic activity under ambient conditions can also be considered as a result of competition between oxygen and *Rz/Rf* reduction. It was demonstrated on C_3N_4 system that photocatalytic activity increased significantly after covering by tape, which effectively excluded oxygen. On the other hand, the same study has not confirmed such effects for TiO_2 , CdS, and WO_3 [85].

3.2.3. Surface wettability under *UV* and visible light

Although very simple for instrumentation, contact angle measurements can provide useful information about the macroscopic wettability of bandgap-reduced ZnO treated glass surfaces. The light-induced amphiphilic phenomenon, i.e., marked change in wettability of the metal oxide surface by water after *UV*-light exposure from hydrophobic to hydrophilic followed by recovery after being stored in the dark was reported for TiO_2 at the end of the last millennium [86]. In fact, the synergy between light-induced hydrophilicity and photocatalysis is the basis for sustaining the self-cleaning ability of TiO_2 which has found many commercial applications. While organic and inorganic pollutants decomposed at semiconductor surface due to photocatalytic mediated redox reaction under *UV* light, photo-induced hydrophilicity reduces the water contact angle facilitating a contaminant removal from the surface by rainwater or moisture. Light-induced hydrophilicity is not inherent to TiO_2 , but it was also observed for other transition metal oxides, including ZnO [87]. The underlying mechanism at the atomic level is

based on photogenerated holes, which may diffuse to the surface where they are trapped at the oxygen lattice sites. Besides direct reaction with pollutants or participation in *ROS* formation, a small portion of trapped holes may attack the photocatalyst itself, breaking the metal-oxygen ions lattice bond by the coordination of the water molecule at a metal site. The coordinated water molecule releases proton for charge compensation, and a new hydroxyl group forms at the surface of the photocatalyst. An increase of the amount of hydroxyl groups at the surface of the photocatalyst is believed to be responsible for light-induced hydrophilicity. However, a newly formed hydrophilic surface is metastable, i.e., singly coordinated hydroxyl groups produced by *UV*-light irradiation are thermodynamically less stable than the originally doubly coordinated hydroxyls and are replaced by oxygen after restoration in the dark. Besides the surface chemistry of given photocatalysts, the time needed for such surface reconstruction at the atomic scale depends mainly on oxygen concentration and humidity of the environment. In order to investigate the light-induced change in wettability behavior, contact angles of blank glass, ZnO₂, and band-gap-reduced ZnO treated glass surfaces were measured after long-term storage in the dark and then after exposure to *UV*-light irradiation (UVP-XX-15BLB, 15 W, PN 95-0042-11, Analytik Jena) for 1 h. After that, the contact angles of prepared substrates were measured at a selected time intervals, being kept in the dark in the meantime, to investigate reversible behavior. Measured values (see Supplement 19) are shown graphically in **Fig. 14a**.

It can be seen that the surface of the blank glass is relatively hydrophilic in the dark with a contact angle of about 23°, while the treated surfaces exhibit much higher contact angle values. These values increase with decreasing annealing temperatures from 65° for the sample ZnO-500 to almost 100° for ZnO-200. After the *UV*-light exposure, the contact angle of the blank glass increased to approximately 60° and remained at the same value after being stored in the dark for 24 h. A typical light-induced hydrophilic behavior can be observed for sample ZnO-500. A drop of liquid spread out completely immediately after being dropped onto the *UV*-light irradiated surface. The first drop with measurable contact angle of about 10° was obtained after 30 min of recovery in the dark, and this value approximately doubled after 1 h in the dark. After 24 h in the dark, contact angle level-off slowly reaching of about 60% of the initial value measured before the *UV*-light exposure. In contrast, such light-induced hydrophilicity was not observed for samples ZnO-200 and even for sample ZnO-300, indicating the existence of ZnO phase in the poorly crystalline and intermediate state. It should be noticed that sample ZnO-300 was highly active in degradation of the photocatalytic *Rz* based ink motif under the *UV* light, which evidently does not correspond to the light-induced hydrophilic behavior.

Similarly, the evaluation of the photocatalytic activity and the contact angle measurement were performed under visible light irradiation using the same light source and cut-on filter which effectively inhibits any *UV* light. Measured values are given in Supplement 20. As can be seen at first sight in **Fig. 14b**, the visible-light irradiation did not induce hydrophilicity even for sample ZnO-500, which should be expected to response because of favorable bandgap energy.

It must be noted, that the variance manifested in the size of error bars in **Fig. 14 a**, and **b** is also a property of prepared samples. The two samples with large variability in contact angle are ZnO₂ and ZnO-200. ZnO₂ is as-obtained and a ZnO-200 is intermediate product on the half-way from peroxide-to-oxide. It is reasonable to expect the quality and uniformity of their surfaces to vary in a much larger way than for the annealed samples. The effect is of moderate intensity in sample ZnO-300. Samples annealed above 300 °C exhibit much smaller error in the contact angle measurement and may have better surface quality and uniformity. This effect is more pronounced for exposition of the samples to *UV* than to visible light. As observed, the visible light causes smaller changes of the contact angle than *UV* light and, indeed, the same effect is manifested for the contact angle variability.

3.2.4. Evaluation of antibacterial activity in dark and under simulated solar light irradiation

Antibacterial activity of the bandgap-reduced ZnO treated glass surface was tested according to the ISO 22196: 2007 with a slight modification described in the experimental section. The results of the number of viable bacteria per cm^2 of sample (CFU/cm^2) and the values of antibacterial activity (R) against the growth of *S. aureus* and *E. coli* are given in **Table 3**.

All tested samples showed strong antibacterial activity against both tested bacterial strains, i.e., against gram-negative bacteria *E. coli* and gram-positive *S. aureus* both in incubation with exposure of samples and in incubation in the dark (see **Tables 3** and **4** and Supplements **21,22**). Since the bacterial counting method error is ± 0.5 of logarithmic order, an antibacterial agent can be considered effective if $R > 1$. It is well known that ZnO exhibits significant antibacterial activity, which is ascribed to synergic effect of reactive oxygen species (*ROS*) mediated destruction of bacterial cells membrane and Zn^{2+} ions mediated disrupted a transcription of mRNA. The release of a small amount of zinc ions to a surrounding environment is due to the little yet detectable solubility of ZnO in water even at neutral pH. Moreover, solubility increases at both low and high pH because ZnO is amphoteric in nature. Our findings support rather effect of zinc ions to be predominant as it seems that contribution of photocatalytic effect is negligible. Under the given testing conditions, same values of antibacterial activities were obtained independently in both dark and light exposure tests. However, it cannot be concluded based solely on values given in **Table 3**. that there is no contribution of photocatalytic activity to antibacterial mechanism. For better insight into the contribution to antibacterial inhibition mechanism, antibacterial tests should be repeated with higher concentration of bacterial suspensions. Similarly, to bandgap-reduced ZnO, also the glass treated by ZnO_2 precursor exhibit strong antibacterial activity against both species. In this case, the antibacterial activity is attributed to the release of hydrogen peroxide, H_2O_2 , which can be readily converted to more potent *ROS*. The dissociation reaction of ZnO_2 takes place intensively at narrow pH between 4 and 6, and besides hydrogen peroxide, Zn^{2+} as a dissolution product contributes to the antibacterial activity as well [88,89].

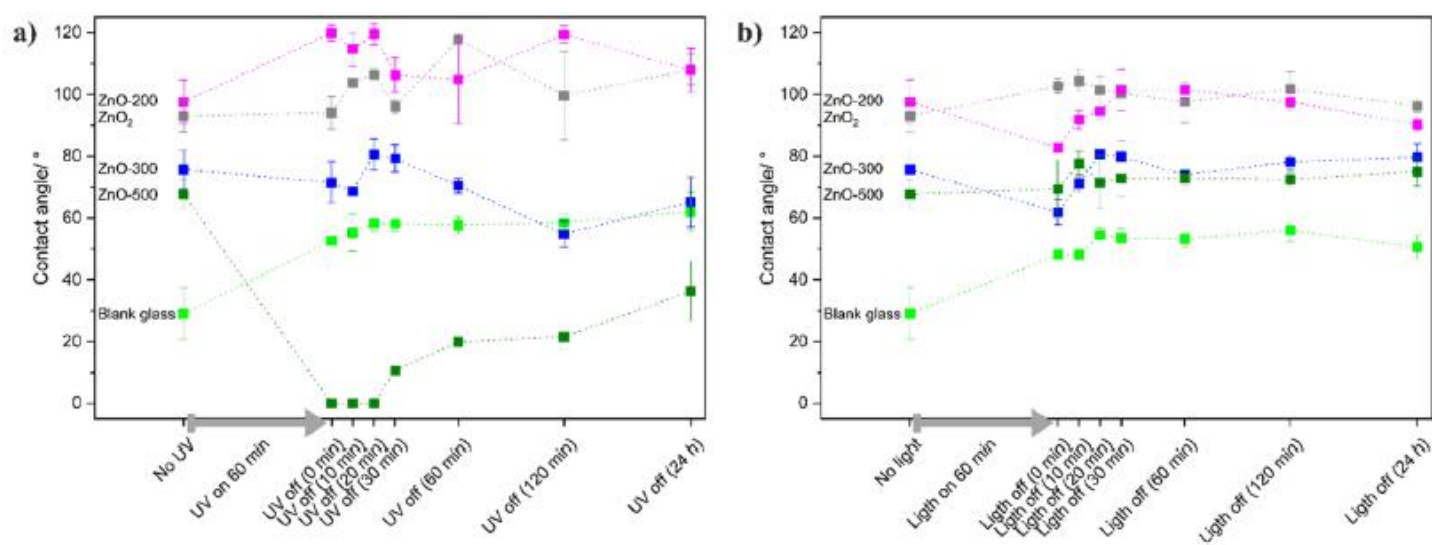


Fig. 14. Contact angle measurements of blank glass, ZnO_2 , and bandgap-reduced ZnO treated glass surface under UV-light irradiation (a) and under visible-light irradiation (b).

Table 3 Results of antibacterial activity evaluation.

Sample		<i>Staphylococcus aureus</i> CGM 4516		<i>Escherichia coli</i> CGM 4517	
		N (CFU/ cm ²)	R = U _t - A _t	N (CFU/ cm ²)	R = U _t - A _t
Untreated glass, (blank)	Rinsed immediately	2.1 × 10 ⁴	(U ₀ = 4.3)	9.3 × 10 ³	(U ₀ = 4.0)
	Incubation with exposure	5.1 × 10 ³	–	5.6 × 10 ⁵	–
ZnO ₂	Incubation in the dark	1.1 × 10 ⁴	(U _t = 4.0)	5.4 × 10 ⁵	(U _t = 5.7)
	Incubation with exposure	< 1	≥ 4.0	< 1	≥ 5.7
ZnO-200	Incubation in the dark	< 1	≥ 4.0	< 1	≥ 5.7
	Incubation with exposure	< 1	≥ 4.0	< 1	≥ 5.7
ZnO-300	Incubation in the dark	< 1	≥ 4.0	< 1	≥ 5.7
	Incubation with exposure	< 1	≥ 4.0	< 1	≥ 5.7
ZnO-500	Incubation in the dark	< 1	≥ 4.0	< 1	≥ 5.7
	Incubation with exposure	< 1	≥ 4.0	< 1	≥ 5.7

R - the antibacterial activity

U_t - the average of the common logarithm of the number of viable bacteria in cells/cm² recovered from the untreated test specimens after 24 h

A_t - the average of the common logarithm of the number of viable bacteria in cells/cm² recovered from the treated test specimens after 24 h

N - the number of viable bacteria recovered per cm² per test specimen.

Table 4 Effectiveness of antibacterial properties.

Effectiveness of antibacterial properties	Value of antibacterial effect R
Weak	1 < R < 2
Significant*	2 ≤ R < 3
Strong*	R ≥ 3

* Values and effectiveness took from ČSN EN ISO 20743: 2014.

4. Conclusions

Thermal decomposition of the ZnO₂ precursor was shown as an efficient way for the preparation of bandgap-reduced ZnO nanocrystal assembly photocatalyst both in the form of powder and thin film on a glass substrate. The precursor can be easily prepared by recrystallization of ZnO dissolved in a mixture of ammonia and hydrogen peroxide. The red and blue shifts of the absorption edge in dependence on the annealing temperature were described. The combined Raman and ESR

spectroscopy study revealed that the bandgap reduction is due to oxygen vacancies. The photocatalytic performance of the prepared sample series was investigated in close vicinities of samples' bandgaps. The 377, 401, and 429 nm wavelengths were chosen for monitoring the *MV* 2B discolouration reaction. The ZnO-ref achieves a higher discolouration rate than bandgap-reduced ZnO samples when irradiated at 377 and 401 nm, while bandgap-reduced samples outperformed ZnO-ref by order of magnitude at 429 nm diode, yet this effect is almost negligible. Photocatalytic experiments using scavengers support the model that oxygen vacancies easily trap photo-excited electrons (whether the V_0^+ or V_0^{++} state) and, if the energy level of this donor state is close enough, the trapped electron could easily thermalize to the conduction band as well as recombine with photo-excited holes.

There are two opposite traits of the observed effects. First, the introduction of oxygen vacancies causes a slight narrowing of the bandgap, which is a beneficial change in the extension of the photocatalytic activity to the visible range, although this effect includes almost only blue light. In addition, the vacancies may also trap photoexcited electrons, which can be helpful in the separation of electron-hole pairs. Finally, if the trapped electron thermalizes from the shallow trap to the conduction band, it can also contribute to photocatalytic activity. On the other hand, futile recombinations of trapped electrons with holes have a detrimental effect on photocatalysis. The electrons may also be trapped in deep traps, which impedes photocatalysis. Both cases diminish the photocatalytic activity in the UV as well as in the visible range. To summarize, involving vacancies in the design of ZnO photocatalysts may have positive and negative effects, and this tradeoff may not always be beneficial as the losses may outweigh the gains, and the overall photocatalytic activity may diminish.

Moreover, photocatalytic activities of bandgap-reduced ZnO easily prepared by annealing ZnO₂ nanocrystal recrystallized directly onto the glass substrate were assessed by monitoring the rate of resazurin reduction in a motif layer indicating a photocatalytically-induced selfcleaning ability of the functionalized glass. Optimal samples were shown effective under *UV*-light irradiation, whereas the photocatalytic activity was weak in the visible-light region. The wettability study of functionalized glass provided yet another indirect evidence of the inability of bandgap-reduced ZnO to become activated under visible-light irradiation. Finally, testing of the antibacterial activity of bandgap-reduced ZnO-treated glass surfaces against *Staphylococcus aureus* and *Escherichia coli* shows that all treated glass surfaces, including ZnO₂ precursor treated, exhibited excellent antibacterial activity under simulated solar light irradiation and even in the dark, indicating mechanism of antibacterial action other than photocatalytic.

References

- [1] K. Hashimoto, H. Irie, A. Fujishima, TiO₂ photocatalysis: a historical overview and future prospects, *Jpn. J. Appl. Phys. Part 1 Regul. Pap. Brief Commun. Rev. Pap.* 44 (2005) 8269-8285, <https://doi.org/10.1143/JJAP.44.8269>.
- [2] D. Spasiano, R. Marotta, S. Malato, P. Fernandez-Ibanez, I. Di Somma, Solar photocatalysis: Materials, reactors, some commercial, and pre-industrialized applications. A comprehensive approach, *Appl. Catal. B Environ.* 170 (2015) 90-123, <https://doi.org/10.1016/j.apcatb.2014.12.050>.
- [3] L. Yao, J. He, Recent progress in antireflection and self-cleaning technology - from surface engineering to functional surfaces, *Prog. Mater. Sci.* 61 (2014) 94-143, <https://doi.org/10.1016/j.pmatsci.2013.12.003>.

- [4] ASTM G173-03 (Standard Tables for Reference Solar Spectral Irradiances: Direct Normal and Hemispherical on 37° Tilted Surface), 2012.
- [5] S. Rehman, R. Ullah, A.M. Butt, N.D. Gohar, Strategies of making TiO₂ and ZnO visible light active, *J. Hazard. Mater.* 170 (2009) 560-569, <https://doi.org/10.1016/j.jhazmat.2009.05.064>.
- [6] A.B. Djuricic, Y. He, A.M.C. Ng, Visible-light photocatalysts: prospects and challenges, *Appl. Mater.* 8 (2020), 030903, <https://doi.org/10.1063/L5140497>.
- [7] G. Reginato, L. Zani, M. Calamante, A. Mordini, A. Dessi, Dye-sensitized heterogeneous photocatalysts for green redox reactions, *Eur. J. Inorg. Chem.* 2020 (2020) 899-917, <https://doi.org/10.1002/ejic.201901174>.
- [8] J. Ge, Y. Zhang, S. Park, Recent advances in carbonaceous photocatalysts with enhanced photocatalytic performances: a mini review, *Materials* 12 (2019) 1916, <https://doi.org/10.3390/ma12121916>.
- [9] Q. Xu, L. Zhang, J. Yu, S. Wageh, A.A. Al-Ghamdi, M. Jaroniec, Direct Z-scheme photocatalysts: Principles, synthesis, and applications, *Mater. Today* 21 (2018) 1042-1063, <https://doi.org/10.1016/j.mattod.2018.04.008>.
- [10] X. Liu, J. Iocozzia, Y. Wang, X. Cui, Y. Chen, S. Zhao, Z. Li, Z. Lin, Noble metal-metal oxide nanohybrids with tailored nanostructures for efficient solar energy conversion, photocatalysis and environmental remediation, *Energy Environ. Sci.* 10 (2017) 402-434, <https://doi.org/10.1039/c6ee02265k>.
- [11] R. Marschall, L. Wang, Non-metal doping of transition metal oxides for visible-light photocatalysis, *Catal. Today* 225 (2014) 111-135, <https://doi.org/10.1016/j.cattod.2013.10.088>.
- [12] V. Kurnaravel, S. Mathew, J. Bartlett, S.C. Pillai, Photocatalytic hydrogen production using metal doped TiO₂: a review of recent advances, *Appl. Catal. B Environ.* 244 (2019) 1021-1064, <https://doi.org/10.1016/j.apcatb.2018.11.080>.
- [13] J. Zhang, K. Tse, M. Wong, Y. Zhang, J. Zhu, A brief review of co-doping, *Front. Phys.* 11 (2016), 117405, <https://doi.org/10.1007/s11467-016-0577-2>.
- [14] T. Sano, N. Mera, Y. Kanai, C. Nishimoto, S. Tsutsui, T. Hirakawa, N. Negishi, Origin of visible-light activity of N-doped TiO₂ photocatalyst: behaviors of N and S atoms in a wet N-doping process, *Appl. Catal. B Environ.* 128 (2012) 77-83, <https://doi.org/10.1016/j.apcatb.2012.06.034>.
- [15] J.Z. Bloh, R. Dillert, D.W. Bahnemann, Designing optimal metal-doped photocatalysts: correlation between photocatalytic activity, doping ratio, and particle size, *J. Phys. Chem. C* 116 (2012) 25558-25562, <https://doi.org/10.1021/jp307313z>.
- [16] Z. Pei, L. Ding, J. Hu, S. Weng, Z. Zheng, M. Huang, P. Liu, Defect and its dominance in ZnO films: a new insight into the role of defect over photocatalytic activity, *Appl. Catal. B Environ.* 142 (2013) 736-743, <https://doi.org/10.1016/j.apcatb.2013.05.055>.
- [17] Z. Xiu, M. Guo, T. Zhao, K. Pan, Z. Xing, Z. Li, W. Zhou, Recent advances in Ti³⁺ self-doped nanostructured TiO₂ visible light photocatalysts for environmental and energy applications, *Chem. Eng. J.* 382 (2020), 123011, <https://doi.org/10.1016/j.cej.2019.123011>.

- [18] A. Janotti, C.G. Van de Walle, Fundamentals of zinc oxide as a semiconductor, *Rep. Prog. Phys.* 72 (2009), 126501, <https://doi.org/10.1088/0034-4885/72/12/126501>.
- [19] K. Tang, S. Gu, J. Ye, S. Zhu, R. Zhang, Y. Zheng, Recent progress of the native defects and p-type doping of zinc oxide, *Chin. Phys. B* 26 (2017), 047702, <https://doi.org/10.1088/1674-1056/26/4/047702>.
- [20] B. Chavillon, L. Cario, A. Renaud, F. Tessier, F. Chevre, M. Boujtita, Y. Pellegrin, E. Blart, A. Smeigh, L. Hammarstrom, F. Odobel, S. Jobic, P-type nitrogen-doped ZnO nanoparticles stable under ambient conditions, *J. Am. Chem. Soc.* 134 (2012) 464-470, <https://doi.org/10.1021/ja208044k>.
- [21] J.E. Eixenberger, C.B. Anders, K. Wada, K.M. Reddy, R.J. Brown, J. Moreno-Ramirez, A.E. Weltner, C. Karthik, D.A. Tenne, D. Fologea, D.G. Wingett, Defect engineering of ZnO nanoparticles for bioimaging applications, *ACS Appl. Mater. Interfaces* 11 (2019) 24933-24944, <https://doi.org/10.1021/acsami.9b01582>.
- [22] V.L. Prasanna, R. Vijayaraghavan, Insight into the mechanism of antibacterial activity of ZnO: surface defects mediated reactive oxygen species even in the dark, *Langmuir* 31 (2015) 9155-9162, <https://doi.org/10.1021/acs.langmuir.5b02266>.
- [23] J. Wang, R. Chen, L. Xiang, S. Komarneni, Synthesis, properties and applications of ZnO nanomaterials with oxygen vacancies: a review, *Ceram. Int.* 44 (2018) 7357-7377, <https://doi.org/10.1016/j.ceramint.2018.02.013>.
- [24] J. Wang, Z. Wang, B. Huang, Y. Ma, Y. Liu, X. Qin, X. Zhang, Y. Dai, Oxygen vacancy induced band-gap narrowing and enhanced visible light photocatalytic activity of ZnO, *ACS Appl. Mater. Interfaces* 4 (2012) 4024-4030, <https://doi.org/10.1021/am300835p>.
- [25] Y. Tang, H. Zhou, K. Zhang, J. Ding, T. Fan, D. Zhang, Visible-light-active ZnO via oxygen vacancy manipulation for efficient formaldehyde photodegradation, *Chem. Eng. J.* 262 (2015) 260-267, <https://doi.org/10.1016/j.cej.2014.09.095>.
- [26] S.Y. Gao, F. Yang, C.J. Song, Q. Cai, R.Y. Wang, S.J. Zhou, Y. Kong, Photocatalytic producing dihydroxybenzenes from phenol enabled by gathering oxygen vacancies in ultrathin porous ZnO nanosheets, *Appl. Surf. Sci.* 505 (2020), <https://doi.org/10.1016/j.apsusc.2019.144580>.
- [27] Y.C. Xu, H.Z. Li, B.J. Sun, P.Z. Qiao, L.P. Ren, G.H. Tian, B.J. Jiang, K. Pan, W. Zhou, Surface oxygen vacancy defect-promoted electron-hole separation for porous defective ZnO hexagonal plates and enhanced solar-driven photocatalytic performance, *Chem. Eng. J.* 379 (2020), <https://doi.org/10.1016/j.cej.2019.122295>.
- [28] Y. Lv, W. Yao, X. Ma, C. Pan, R. Zong, Y. Zhu, The surface oxygen vacancy induced visible activity and enhanced UV activity of a ZnO_{1-x} photocatalyst, *Catal. Sci. Technol.* 3 (2013) 3136-3146, <https://doi.org/10.1039/c3cy00369h>.
- [29] Y. Lv, C. Pan, X. Ma, R. Zong, X. Bai, Y. Zhu, Production of visible activity and UV performance enhancement of ZnO photocatalyst via vacuum deoxidation, *Appl. Catal. B Environ.* 138 (2013) 26-32, <https://doi.org/10.1016/j.apcatb.2013.02.011>.
- [30] Y. Peng, Y. Wang, Q. Chen, Q. Zhub, A.W. Xu, Stable yellow ZnO mesocrystals with efficient visible-light photocatalytic activity, *CrystEngComm* 16 (2014) 7906-7913, <https://doi.org/10.1039/c4ce00695j>.

- [31] D. Chen, Z. Wang, T. Ren, H. Ding, W. Yao, R. Zong, Y. Zhu, Influence of defects on the photocatalytic activity of ZnO, *J. Phys. Chem. C* 118 (2014) 15300-15307, <https://doi.org/10.1021/jp5033349>.
- [32] M. Lau, S. Reichenberger, I. Haxhijaj, S. Barcikowski, A.M. Muller, Mechanism of laser-induced bulk and surface defect generation in ZnO and TiO₂ nanoparticles: effect on photoelectrochemical performance, *ACS Appl. Energy Mater.* 1 (2018) 5366-5385, <https://doi.org/10.1021/acsaem.8b00977>.
- [33] Z.S. Li, X.H. Liu, M. Zhou, S.L. Zhang, S.Z. Cao, G.L. Lei, C.M. Lou, J. Zhang, Plasma-induced oxygen vacancies enabled ultrathin ZnO films for highly sensitive detection of triethylamine, *J. Hazard. Mater.* 415 (2021), <https://doi.org/10.1016/j.jhazmat.2021.125757>.
- [34] J. Sedlak, I. Kuritka, M. Masar, M. Machovsky, P. Urbanek, P. Bazant, P. Janota, M. Dvorackova, Contributions of morphological and structural parameters at different hierarchical morphology levels to photocatalytic activity of mesoporous nanostructured ZnO, *Appl. Surf. Sci.* 513 (2020), 145773, <https://doi.org/10.1016/j.apsusc.2020.145773>.
- [35] H. Ali, A.C. Guler, M. Masar, P. Urbanek, M. Urbanek, D. Skoda, P. Suly, M. Machovsky, D. Galusek, I. Kuritka, Solid-state synthesis of direct Z-scheme Cu₂O/WO₃ nanocomposites with enhanced visible-light photocatalytic performance, *Catalysts* 11 (2021), <https://doi.org/10.3390/catal11020293>.
- [36] ISO 21066:2018 Fine Ceramics (Advanced Ceramics, Advanced Technical Ceramics) — Qualitative and Semiquantitative Assessment of the Photocatalytic Activities of Surfaces by the Reduction of Resazurin in A Deposited Ink Film.
- [37] ISO 22196:2011 Measurement of Antibacterial Activity on Plastics and Other Nonporous Surfaces.
- [38] T. Daley, K.B. Opuni, E. Raj, A.J. Dent, G. Cibir, T. Hyde, I.G. Sankar, Monitoring the process of formation of ZnO from ZnO₂ using in situ combined XRD/XAS technique, *J. Phys. Condens. Matter* 33 (2021), 264002, <https://doi.org/10.1088/1361-648X/abfb91>.
- [39] A. Escobedo-Morales, D. Tellez-Flores, M.d.L. Ruiz Peralta, J. Garcia-Serrano, A.M. Herrera-Gonzalez, E. Rubio-Rosas, E. Sanchez-Mora, O. Olivares Xometl, Green method for producing hierarchically assembled pristine porous ZnO nanoparticles with narrow particle size distribution, *Mater. Chem. Phys.*, 151, 2015, pp. 282-287. (DOI: [10.1016/j.matchemphys.2014.11.067](https://doi.org/10.1016/j.matchemphys.2014.11.067)).
- [40] M. Sun, W. Hao, C. Wang, T. Wang, A simple and green approach for preparation of ZnO₂ and ZnO under sunlight irradiation, *Chem. Phys. Lett.* 443 (2007) 342-346, <https://doi.org/10.1016/j.cplett.2007.06.098>.
- [41] H. EYSEL, S. THYM, Raman-spectra of peroxides, *Z. Anorg. Allg. Chem.* 411 (1975) 97-102, <https://doi.org/10.1002/zaac.19754110202>.
- [42] V. Vacque, B. Sombret, J. Huvenne, P. Legrand, S. Suc, Characterisation of the O-O peroxide bond by vibrational spectroscopy, *Spectrochim. Acta Part A Mol. Biomol. Spectrosc.* 53 (1997) 55-66, [https://doi.org/10.1016/S0584-8539\(96\)01777-1](https://doi.org/10.1016/S0584-8539(96)01777-1).
- [43] H. Fukushima, T. Kozu, H. Shima, H. Funakubo, H. Uchida, T. Katoda, K. Nishida, Evaluation of oxygen vacancy in ZnO using Raman spectroscopy, in: *Proceedings of the 2015 Joint IEEE*

International Symposium on the Applications of Ferroelectric, International Symposium on Integrated Functionalities and Piezoelectric Force Microscopy Workshop (Isaf/isif/pfm), 2015, pp. 28-31.

- [44] Y. Song, S.X. Zhang, C.H. Zhang, Y.T. Yang, K.Y. Lv, Raman spectra and microstructure of zinc oxide irradiated with swift heavy ion, *Crystals* 9 (2019), <https://doi.org/10.3390/cryst9080395>.
- [45] H. Fukushima, H. Uchida, H. Funakubo, T. Katoda, K. Nishida, Evaluation of oxygen vacancies in ZnO single crystals and powders by micro-Raman spectroscopy, *J. Ceram. Soc. Jpn.* 125 (2017) 445-448, <https://doi.org/10.2109/jcersj2.16262>.
- [46] E.H. Hasdeo, A. Nugraha, M.S. Dresselhaus, R. Saito, Breit-Wigner-Fano line shapes in Raman spectra of graphene, *Phys. Rev. B* 90 (2014), <https://doi.org/10.1103/PhysRevB.90.245140>.
- [47] Y.K. Kim, H.M. Jang, Raman line-shape analysis of nano-structural evolution in cation-ordered ZrTiO₄-based dielectrics, *Solid State Commun.* 127 (2003) 433-437, [https://doi.org/10.1016/S0038-1098\(03\)00463-0](https://doi.org/10.1016/S0038-1098(03)00463-0).
- [48] J.B. Wang, H.M. Zhong, Z.F. Li, W. Lu, Raman study for E-2 phonon of ZnO in Zn_{1-x}Mn_xO nanoparticles, *J. Appl. Phys.* 97 (2005), <https://doi.org/10.1063/1.1865340>.
- [49] I. Kosacki, T. Suzuki, H.U. Anderson, P. Colomban, Raman scattering and lattice defects in nanocrystalline CeO₂ thin films, *Solid State Ion.* 149 (2002) 99-105, [https://doi.org/10.1016/S0167-2738\(02\)00104-2](https://doi.org/10.1016/S0167-2738(02)00104-2).
- [50] G.S. Dev, V. Sharma, A. Singh, V.S. Baghel, M. Yanagida, A. Nagataki, N. Tripathi, Raman spectroscopic study of ZnO/NiO nanocomposites based on spatial correlation model, *RSC Adv.* 9 (2019) 26956-26960, <https://doi.org/10.1039/c9ra04555d>.
- [51] P.H. Shih, S.Y. Wu, The influence of short-range correlation on the phonon confinement of a single ZnO nanowire, *Nanoscale Res. Lett.* 12 (2017), <https://doi.org/10.1186/s11671-017-2013-0>.
- [52] N. Tripathi, K Vijayarangamuthu, S. Rath, A Raman spectroscopic study of structural evolution of electrochemically deposited ZnO films with deposition time, *Mater. Chem. Phys.* 126 (2011) 568-572, <https://doi.org/10.1016/j.matchemphys.2011.01.026>.
- [53] J.B. Wang, H.M. Zhong, Z.F. Li, W. Lu, Raman study for E-2 phonon of ZnO in Zn_{1-x}Mn_xO nanoparticles, *J. Appl. Phys.* 97 (2005), <https://doi.org/10.1063/1.1865340>.
- [54] R. Cusco, E. Alarcon-Llado, J. Ibanez, L. Artus, J. Jimenez, B. Wang, M.J. Callahan, Temperature dependence of raman scattering in ZnO, *Phys. Rev. B* 75 (2007), 165202, <https://doi.org/10.1103/PhysRevB.75.165202>.
- [55] A. Souissi, C. Sartel, G. Amiri, A. Meftah, A. Lusson, P. Galtier, V. Sallet, M. Oueslati, Raman study of activated quasi-modes due to misorientation of ZnO nanowires, *Solid State Commun.* 152 (2012) 1729-1733, <https://doi.org/10.1016/j.ssc.2012.06.004>.
- [56] A. Janotti, C.G. Van de Walle, Native point defects in ZnO, *Phys. Rev. B* 76 (2007), 165202, <https://doi.org/10.1103/PhysRevB.76.165202>.

- [57] K. Tang, S. Gu, J. Ye, S. Zhu, R. Zhang, Y. Zheng, Recent progress of the native defects and p-type doping of zinc oxide, *Chin. Phys. B* 26 (2017), 047702, <https://doi.org/10.1088/1674-1056/26/4/047702>.
- [58] M.D. McCluskey, S.J. Jokela, Defects in ZnO, *J. Appl. Phys.* 106 (2009), 071101, <https://doi.org/10.1063/1.3216464>.
- [59] A. Janotti, C. Van de Walle, Oxygen vacancies in ZnO, *Appl. Phys. Lett.* 87 (2005), 122102, <https://doi.org/10.1063/L2053360>.
- [60] L. Vlasenko, G. Watkins, Optical detection of electron paramagnetic resonance for intrinsic defects produced in ZnO by 2.5-MeV electron irradiation in situ at 4.2 K, *Phys. Rev. B* 72 (2005), 035203, <https://doi.org/10.1103/PhysRevB.72.035203>.
- [61] V. Ischenko, S. Polarz, D. Grote, V. Stavarache, K. Fink, M. Driess, Zinc oxide nanoparticles with defects, *Adv. Funct. Mater.* 15 (2005) 1945-1954, <https://doi.org/10.1002/adfm.200500087>.
- [62] G. Neumann, On the defect structure of zinc-doped zinc-oxide, *Phys. Status Solidi B Basic Res.* 105 (1981) 605-612, <https://doi.org/10.1002/pssb.2221050220>.
- [63] L.E. Halliburton, N.C. Giles, N.Y. Garces, M. Luo, C.C. Xu, L.H. Bai, L.A. Boatner, Production of native donors in ZnO by annealing at high temperature in Zn vapor, *Appl. Phys. Lett.* 87 (2005), 172108, <https://doi.org/10.1063/L2117630>.
- [64] A. Poppl, G. Volkel, ESR investigation of the oxygen vacancy in pure and Bi₂O₃-doped ZnO ceramics, *Phys. Status Solidi A Appl. Res.* 115 (1989) 247-255, <https://doi.org/10.1002/pssa.2211150127>.
- [65] L. Liu, Z. Mei, A. Tang, A. Azarov, A. Kuznetsov, Q. Xue, X. Du, Oxygen vacancies: the origin of n-type conductivity in ZnO, *Phys. Rev. B* 93 (2016), 235305, <https://doi.org/10.1103/PhysRevB.93.235305>.
- [66] S. Polarz, J. Strunk, V. Ischenko, M.W.E. van den Berg, O. Hinrichsen, M. Muhler, M. Driess, On the role of oxygen defects in the catalytic performance of zinc oxide, *Angew. Chem. Int. Ed.* 45 (2006) 2965-2969, <https://doi.org/10.1002/anie.200503068>.
- [67] K. Vanheusden, W. Warren, C. Seager, D. Tallant, J. Voigt, B. Gnade, Mechanisms behind green photoluminescence in ZnO phosphor powders, *J. Appl. Phys.* 79 (1996) 7983-7990, <https://doi.org/10.1063/L362349>.
- [68] R. Iyengar, V. Rao, Electron spin resonance studies on zinc peroxide and on zinc oxide obtained from a decomposition of zinc peroxide, *J. Phys. Chem.*, 75, 1971, pp. 3089-&. (DOI: [10.1021/j100689a009](https://doi.org/10.1021/j100689a009)).
- [69] K. Vanheusden, C. Seager, W. Warren, D. Tallant, J. Voigt, Correlation between photoluminescence and oxygen vacancies in ZnO phosphors, *Appl. Phys. Lett.* 68 (1996) 403-405, <https://doi.org/10.1063/L116699>.
- [70] V. Srikant, D. Clarke, On the optical band gap of zinc oxide, *J. Appl. Phys.* 83 (1998) 5447-5451, <https://doi.org/10.1063/L367375>.
- [71] P.A. Rodnyi, I.V. Khodyuk, Optical and luminescence properties of zinc oxide (review), *Opt. Spectrosc.* 111 (2011) 776-785, <https://doi.org/10.1134/S0030400X11120216>.

- [72] J. Lv, C. Li, Evidences of V-O, V-Zn, and O-i defects as the green luminescence origins in ZnO, *Appl. Phys. Lett.* 103 (2013), 232114, <https://doi.org/10.1063/l.4844735>.
- [73] W. Li, G. Wang, C. Chen, J. Liao, Z. Li, Enhanced visible light photocatalytic activity of ZnO nanowires doped with Mn²⁺ and Co²⁺ ions, *Nanomaterials* 7 (2017), <https://doi.org/10.3390/nano7010020>.
- [74] Y. Ma, T. Choi, S.H. Cheung, Y. Cheng, X. Xu, Y. Xie, H. Li, M. Li, H. Luo, W. Zhang, S.K. So, S. Chen, S. Tsang, Charge transfer-induced photoluminescence in ZnO nanoparticles, *Nanoscale* 11 (2019) 8736-8743, <https://doi.org/10.1039/c9nr02020a>.
- [75] A. Djuricic, W. Choy, V. Roy, Y. Leung, C. Kwong, K. Cheah, T. Rao, W. Chan, H. Lui, C. Surya, Photoluminescence and electron paramagnetic resonance of ZnO tetrapod structure, *Adv. Funct. Mater.* 14 (2004) 856-864, <https://doi.org/10.1002/adfm.200305082>.
- [76] L.Q. Jing, Y.C. Qu, B.Q. Wang, S.D. Li, B.J. Jiang, L.B. Yang, W. Fu, H.G. Fu, J. Z. Sun, Review of photoluminescence performance of nano-sized semiconductor materials and its relationships with photocatalytic activity, *Sol. Energy Mater. Sol. Cells* 90 (2006) 1773-1787, <https://doi.org/10.1016/j.solmat.2005.11.007>.
- [77] N. Uekawa, N. Mochizuki, J. Kajiwara, F. Mori, Y.J. Wu, K. Kakegawa, Nonstoichiometric properties of zinc oxide nanoparticles prepared by decomposition of zinc peroxide, *Phys. Chem. Chem. Phys.* 5 (2003) 929-934, <https://doi.org/10.1039/b210990e>.
- [78] H. Ali, A.C. Guler, M. Masar, P. Urbanek, M. Urbanek, D. Skoda, P. Suly, M. Machovsky, D. Galusek, I. Kuritka, Solid-State Synthesis of Direct Z-Scheme Cu₂O/WO₃ Nanocomposites with Enhanced Visible-Light Photocatalytic Performance, 11, 2021.
- [79] S. Morrison, T. Freund, Chemical role of holes and electrons in ZnO photocatalysis, *J. Chem. Phys.* 47 (1967) 1543. & doi:10.1063/1.1712115.
- [80] A. Mills, D. Yusufu, N. Wells, C. O'Rourke, Assessment of activity of 'transparent and clear' and 'opaque and highly coloured' photocatalytic samples using a fluorescent photocatalytic activity indicator ink, *FPaii, J. Photochem. Photobiol. A Chem.* 330 (2016) 90-94, <https://doi.org/10.1016/j.jphotochem.2016.07.019>.
- [81] A. Mills, J. Wang, S. Lee, M. Simonsen, An intelligence ink for photocatalytic films, *Chem. Commun.* (2005) 2721-2723, <https://doi.org/10.1039/b501131k>.
- [82] A. Mills, N. Wells, Reductive photocatalysis and smart inks, *Chem. Soc. Rev.* 44 (2015) 2849-2864, <https://doi.org/10.1039/c4cs00279b>.
- [83] N. Barbero, D. Vione, Why dyes should not be used to test the photocatalytic activity of semiconductor oxides, *Environ. Sci. Technol.* 50 (2016) 2130-2131, <https://doi.org/10.1021/acs.est.6b00213>.
- [84] M. Rochkind, S. Pasternak, Y. Paz, Using dyes for evaluating photocatalytic properties: a critical review, *Molecules* 20 (2015) 88-110, <https://doi.org/10.3390/molecules20010088>.
- [85] A. Mills, N. Wells, C. O'Rourke, Probing the activities of UV and visible-light absorbing photocatalyst powders using a resazurin-based photocatalyst activity indicator ink (Rz Paii), *J. Photochem. Photobiol. A Chem.* 338 (2017) 123-133, <https://doi.org/10.1016/j.jphotochem.2017.01.030>.

- [86] R. Wang, K. Hashimoto, A. Fujishima, M. Chikuni, E. Kojima, A. Kitamura, M. Shimohigoshi, T. Watanabe, Light-induced amphiphilic surfaces, *Nature* 388 (1997) 431-432, <https://doi.org/10.1038/41233>.
- [87] M.G. Krishna, M. Vinjanampati, D.D. Purkayastha, Metal oxide thin films and nanostructures for self-cleaning applications: current status and future prospects, *Eur. Phys. J. Appl. Phys.* 62 (2013) 30001, <https://doi.org/10.1051/epjap/2013130048>.
- [88] Y. Wolanov, P.V. Prikhodchenko, A.G. Medvedev, R. Pedahzur, O. Lev, Zinc dioxide nanoparticulates: a hydrogen peroxide source at moderate pH, *Environ. Sci. Technol.* 47 (2013) 8769-8774, <https://doi.org/10.1021/es4020629>.
- [89] C. Bergs, L. Brueck, R.R. Rosencrantz, G. Conrads, L. Elling, A. Pich, Biofunctionalized zinc peroxide (ZnO₂) nanoparticles as active oxygen sources and antibacterial agents, *RSC Adv.* 7 (2017) 38998-39010, <https://doi.org/10.1039/c7ra06332f>.